

Modeled Three-Dimensional Currents and Eddies on an Alongshore-Variable Barred Beach

Christine M. Baker¹, Melissa Moulton², Britt Raubenheimer³, Steve Elgar³, and Nirnimesh
Kumar¹

¹Department of Civil & Environmental Engineering, University of Washington, Seattle, WA

²Applied Physics Laboratory, University of Washington, Seattle, WA

³Woods Hole Oceanographic Institution, Woods Hole, MA

Key Points:

- Trends in SWASH-simulated nearshore circulation patterns and magnitudes on an alongshore-variable barred beach are similar to observations
- Small length-scale eddies are intensified by wave directional spread, and large eddies are enhanced by alongshore bathymetric variability
- Eddy length scales and low-frequency currents are weakly vertically-dependent in the outer surf zone and depth-uniform in shallower water

Corresponding author: Christine Baker, Ph# 206-221-7623, cmbaker9@uw.edu

Abstract

Circulation in the nearshore region, which is critical for material transport along the coast and between the surf zone and the inner shelf, includes strong vortical motions. The horizontal length scales and vertical structure associated with vortical motions are not well documented on alongshore-variable beaches. Here, a three-dimensional phase-resolving numerical model, Simulating WAVes till SHore (SWASH), is compared with surfzone waves and flows on a barred beach, and is used to investigate surfzone eddies. Model simulations with measured bathymetry reproduce trends in the mean surfzone circulation patterns, including alongshore currents and rip current circulation cells observed for offshore wave heights from 0.5 to 2.0 m and incident wave directions from 0 to 15° relative to shore normal. The length scales of simulated eddies, quantified using the alongshore wavenumber spectra of vertical vorticity, suggest that increasing wave directional spread intensifies small-scale eddies ($O(10)$ m). Simulations with bathymetric variability ranging from alongshore uniform to highly alongshore variable indicate that large-scale eddies ($O(100)$ m) may be enhanced by surfzone bathymetric variability, whereas small-scale eddies ($O(10)$ m) are less dependent on bathymetric variability. The simulated vertical dependence of the magnitude and mean length scale (centroid) of the alongshore wavenumber spectra of vertical vorticity and very low-frequency ($f \approx 0.005$ Hz) currents is weak in the outer surf zone, and decreases toward the shoreline. The vertical dependence in the simulations may be affected by the vertical structure of turbulence, mean shear, and bottom boundary layer dynamics.

Plain Language Summary

The nearshore region includes the surf zone, where waves break, and the inner shelf, which extends several km offshore from the surf zone. Within this region, currents transport contaminants, sediments, and larvae along the coast and between the beach and the shelf. Nearshore eddies are rotational currents that fluctuate at timescales longer than individual waves and shorter than mean hourly currents, and are important to mixing and transport. Here, a three-dimensional numerical model simulates observed waves and flow patterns on a natural beach near Duck, NC with highly variable seafloor elevations (*e.g.*, bumps and holes). Estimates of the alongshore (parallel to the coastline) length of simulated eddies suggest that large eddies are enhanced by higher variability in the seafloor, whereas the intensity of small eddies increases when waves enter the surf zone with larger directional spread (from multiple direc-

tions). The structure and strength of nearshore eddies over the water column is shown to vary across the surf zone.

1 Introduction

The nearshore region consists of the surf zone, extending from the shoreline to the seaward limit of depth-induced wave breaking, and the inner shelf, a region with overlapping surface and bottom boundary layers on the continental shelf offshore of the surf zone [Lentz and Fewings, 2012]. Quantifying circulation dynamics and the transport of material (*e.g.*, contaminants, sediments, and larvae) in the nearshore is critical given the concentration of recreational, commercial, and ecosystem resources in this region [Boehm *et al.*, 2017]. Nearshore currents may dilute or concentrate pollutants and pathogens that cause gastrointestinal infections and require beach closures [Stoner and Dorfman, 2007], and excess nutrient supply from terrestrial runoff may lead to eutrophication in coastal zones, creating hypoxic conditions that threaten benthic organisms and ecosystem health [Boehm *et al.*, 2016]. In addition, species inhabiting the nearshore (*e.g.*, intertidal invertebrate gametes) exploit cross-shore circulation for recruitment and settlement [Shanks *et al.*, 2010; Morgan *et al.*, 2018]. A comprehensive understanding of nearshore dynamics is necessary to maintain public safety and reduce anthropogenic stresses on ecosystems.

Surfzone circulation is the result of complex interactions between surface waves, bathymetric irregularities, and bottom boundary layer dynamics. Mean cross-shore velocities are characterized by a balance between radiation-stress gradients, barotropic-pressure gradients, and a weaker contribution from bottom stress, resulting in wave setup and an offshore near-bed return current [*i.e.*, ‘undertow’, Longuet-Higgins and Stewart, 1964; Bowen *et al.*, 1968; Stive and Wind, 1982; Raubenheimer *et al.*, 2001]. Wave-induced mean alongshore currents result from alongshore barotropic-pressure gradients [Apotsos *et al.*, 2008; Hansen *et al.*, 2015] and cross-shore gradients of the off-diagonal component of the radiation-stress tensor [Longuet-Higgins, 1970; Feddersen *et al.*, 1998; Garcez-Faria *et al.*, 1998], primarily balanced by bottom stress [Visser, 1986; Simons *et al.*, 1992; Reniers *et al.*, 2004a]. Wave breaking over alongshore bathymetric variations drives rip currents and meandering alongshore currents, including cell-like circulation patterns [MacMahan *et al.*, 2006; Dalrymple *et al.*, 2011; Castelle *et al.*, 2016; Moulton *et al.*, 2017].

The vertical structure of surfzone currents depends on the forces associated with surface wave breaking, bottom friction, and interaction with the three-dimensional circulation [Putrevu *et al.*, 1995; MacMahan *et al.*, 2004], and is altered by the vertical distribution of turbulence in the water column, which depends on the breaking wave energy and bed roughness [Feddersen and Trowbridge, 2005; Feddersen, 2012; Henderson *et al.*, 2017]. Field and numerical modeling studies have investigated the vertical profile of undertow [Garcez-Faria *et al.*, 1998] and of mean alongshore currents [Garcez-Faria *et al.*, 2000; Reniers *et al.*, 2004a]. However, the three-dimensional structure of surfzone velocities at timescales longer than those of wind waves (*e.g.*, surfzone eddies) and their implications for material exchange are not understood well.

Surfzone eddy activity contributes to dispersion and mixing, thus affecting the transport of material along the coast and between the surf zone and the inner shelf [Spydell and Feddersen, 2009; Clark *et al.*, 2010, 2011; Suanda and Feddersen, 2015]. Very low-frequency (VLF) vortical motions at timescales greater than 250 s (approximately $f < 0.004$ Hz, where f is frequency), longer than infragravity timescales ($0.004 < f < 0.040$ Hz), may be generated by shear instabilities [Bowen and Holman, 1989; Oltman-Shay *et al.*, 1989; Allen *et al.*, 1996] and wave-breaking induced vorticity [Peregrine, 1998; Haller *et al.*, 1999]. Shear instabilities in a wave-driven alongshore current have been observed with length scales up to several hundred meters [Oltman-Shay *et al.*, 1989]. Wave-group driven alongshore radiation stress gradients from alongshore wave-breaking variability may contribute to surfzone eddy generation with length scales on the order (O) of 100 m [Haller *et al.*, 1999; Reniers *et al.*, 2004b; Long and Özkan Haller, 2009]. As a result of alongshore gradients in wave dissipation, short-crested breaking waves generate vorticity with length scales $O(10)$ m [Peregrine, 1998; Clark *et al.*, 2012], which are hypothesized to coalesce to larger scales $O(100)$ m [Spydell and Feddersen, 2009; Elgar and Raubenheimer, 2020] due to an inverse energy cascade [Kraichnan, 1967; Boffetta and Ecke, 2012]. The length scales associated with vortical motions generated by both shear instabilities and wave breaking have been explored for depth-integrated velocities on alongshore-uniform beaches [Spydell and Feddersen, 2009; Feddersen *et al.*, 2011; Feddersen, 2014; Kumar and Feddersen, 2017] and an alongshore-varying beach [O’Dea *et al.*, 2021], but have not been explored for depth-varying velocities on beaches with complex bathymetry.

Surfzone vortical motions, often assumed to be depth-uniform, usually have been measured at a single elevation with a horizontally spaced sensor array. However, two recent stud-

ies on a barred beach measured low-frequency motions with vertically stacked electromagnetic current sensors [Lippmann *et al.*, 2016] and acoustic Doppler profilers [Henderson *et al.*, 2017]. These studies found that low-frequency cross- and alongshore velocities are weakly vertically dependent in the outer surf zone [Lippmann *et al.*, 2016; Henderson *et al.*, 2017]. Analytic solutions based on bottom boundary layer theory indicate complex vertical structure of low-frequency motions in the presence of a horizontally sheared alongshore current [Lippmann and Bowen, 2016]. Although these studies have established that eddies in the outer surf zone have some vertical variability, further investigation is necessary to understand the vertical dependence of VLF currents for varying beach profiles and wave conditions.

Numerical modeling has been used to investigate the three-dimensionality of surf-zone vortical motions. Phase-averaged models that simulate the evolution of the wave energy spectrum are skillful at reproducing some mean wave-induced dynamics, including rip-current circulation, alongshore currents, and wave setup [Reniers *et al.*, 2004a; Uchiyama *et al.*, 2010; Kumar *et al.*, 2012], but do not include vertical vorticity generated by finite-crested wave breaking. Studies using three-dimensional phase-averaged model simulations indicate that vertical shear instabilities modify depth-dependent currents due to dispersive mixing [Newberger and Allen, 2007a,b], and that VLF motions are excited on complex bathymetry [Uchiyama *et al.*, 2017]. However, the parameterizations of wave-induced vorticity associated with energy dissipation from short-crested wave breaking used in phase-averaged models have not been tested extensively.

Coupled ocean-circulation and phase-averaged wave models (*e.g.*, COAWST) simulate vertically varying surfzone circulation [Warner *et al.*, 2010; Kumar *et al.*, 2012], and can be one-way coupled with depth-averaged phase-resolving models (*e.g.*, funwaveC) to allow for the investigation of three-dimensional eddies resulting from bulk vorticity injection similar to that resulting from short-crested wave breaking [Kumar and Feddersen, 2017]. However, wave-forced rotational flows associated with eddies may be aliased as a result of the 1-Hz model output from the phase-resolving simulations [Kumar and Feddersen, 2017]. In addition, two-way coupled wave-current interactions between three-dimensional eddies and propagating waves are not included.

Phase-resolving Boussinesq models (*e.g.*, FUNWAVE-TVD and funwaveC), which simulate individual wave propagation, have been used to study surfzone vorticity dynamics, including finite-crested wave-breaking eddy generation [Feddersen, 2014; Hally-Rosendahl

and Feddersen, 2016]. These models are depth integrated, and thus do not resolve eddy vertical variability. Three-dimensional phase-resolving non-hydrostatic numerical models, such as Simulating WAVes til SHore (SWASH) and NHWAVE, contain the physics needed to simulate three-dimensional circulation and vorticity dynamics, including wave-forced eddy generation [Zijlema *et al.*, 2011; Derakhti *et al.*, 2016]. SWASH has been used to study nearshore wave breaking, infragravity wave dynamics, nonlinear infragravity-wave interactions, run-up oscillations, and nonlinear wave-dynamics [Rijnsdorp *et al.*, 2012, 2014; Smit *et al.*, 2013; Ruju *et al.*, 2014; Smit *et al.*, 2014; de Bakker *et al.*, 2016]. Although SWASH has skill simulating wave-induced flows measured in the laboratory, including the undertow profile and alongshore currents [Rijnsdorp *et al.*, 2017], the accuracy of SWASH-simulated surfzone circulation on an alongshore-variable beach has not been tested.

Here, SWASH is used to simulate three-dimensional wave propagation and circulation on a beach with complex alongshore-varying bathymetry. The field experiment and model setup are described in section 2, and the results comparing the observed with the simulated wave statistics and circulation patterns are presented in section 3. Additionally, the relative roles of alongshore bathymetric variability and directional spread in the horizontal and depth variability of length scales of the simulated eddies, and of the vertical structure of VLF horizontal velocities, are presented in section 3. The physical processes influencing the horizontal and depth variability of surfzone eddies and VLF currents are discussed in section 4. The results are summarized in section 5.

2 Methods

2.1 Field Experiment

Field observations were collected on an alongshore-inhomogeneous barred beach near Duck, North Carolina at the United States Army Corps of Engineers Field Research Facility (FRF, <http://frf.usace.army.mil/frf.shtml>) as part of the BathyDuck-2015 Experiment, a large effort to evaluate and improve the estimation of surfzone bathymetry [Smith *et al.*, 2017]. Instruments included offshore wave sensors in water depths (h) of 11 ($x, y = 1295, 978$ m, positive offshore and to the north, respectively) and 6 m ($x, y = 606, 937$ m) and an array of colocated pressure sensors and acoustic Doppler velocimeters (ADV) in the surf zone, sampled at 2 Hz (Figure 1a,b). Two cross-shore transects of four colocated ADVs and pressure sensors were deployed from $-3.5 < z < -1.5$ m (positive upward and referenced to the

NAVD88 datum, approximately local mean sea level), initially positioned 0.5 to 1.0 m above the bed, and separated by approximately 125 m in the cross-shore and 75 m in the alongshore (Figure 1, red circles, $y = 741$ and 813 m). Two additional sensors were deployed south of these arrays near the FRF pier ($y = 521$ m). Occasionally, current meter data were omitted when sensors were out of the water (low tide) or buried (accretion).

Bathymetric surveys were performed on Oct. 14 and Nov. 16, 2015 with the Lighter Amphibious Resupply Cargo (LARC) vehicle using a single-beam acoustic sonar and RTK GPS (Figure 1). The survey data were smoothed to an 8-m cross-shore by 45-m alongshore gridded bathymetry with estimated root-mean-square vertical elevation errors of approximately 0.05 m, attributed to sampling and interpolation errors [Plant *et al.*, 2002; Smith *et al.*, 2017]. The surveys covered 1200-m in the alongshore ($y = -100$ – 1100 m) and spanned from the beach to $h \approx 9$ m ($x = 50$ – 950 m).

Between the most offshore position of the shoreline ($x = 135$ m) and the bar crest ($x = 235$ m), the Oct. 14 bathymetry has a maximum surfzone alongshore standard deviation ($\sigma_{y,sz}$) of 0.86 m (Figure 1c, left vertical bar, S3a) located in the trough region. The nondimensional metric of bathymetric nonuniformity (χ^2), the spatially averaged and normalized squared difference between the measured depth ($h(x, y)$) and the alongshore-averaged cross-shore depth ($\bar{h}(x)$) [Ruessink *et al.*, 2001] is defined as:

$$\chi^2 = \frac{1}{L_x L_y} \int_{x_0}^{x_{sz}} \int_{y_{south}}^{y_{north}} \left(\frac{h(x, y) - \bar{h}(x)}{\bar{h}(x)} \right)^2 dy dx \quad (1)$$

where L_x and L_y are the cross-shore and alongshore length where χ^2 is evaluated. χ^2 computed from $x = 134$ m (the farthest offshore extent where $h = 0$ m, x_0) to $x = 260$ m (the edge of the surf zone for the simulations with the largest wave height, x_{sz}) and $-100 \geq y \geq 1100$ m is 0.099. The χ^2 is sensitive to the cross-shore extent over which it is computed and increases for smaller surfzone widths. The χ^2 of the bathymetry observed on Oct 14 is ~ 5 times larger than previous experiments with alongshore bathymetric variations described as small to moderate in Duck, NC and central California [Ruessink *et al.*, 2001; Feddersen and Guza, 2003; O'Dea *et al.*, 2021], and is > 25 times larger than observed on a beach described as alongshore uniform [Spydell and Feddersen, 2009]. On Oct. 14 (Nov. 16), the average shoreline position was approximately $x = 108$ m (110 m), and a single bar was located near $x = 235$ m (215 m) with an alongshore-variable trough near $x = 175$ m (170 m). In both bathymetric surveys, the morphology includes bar-trough patterns (*e.g.*, Figure 1a:

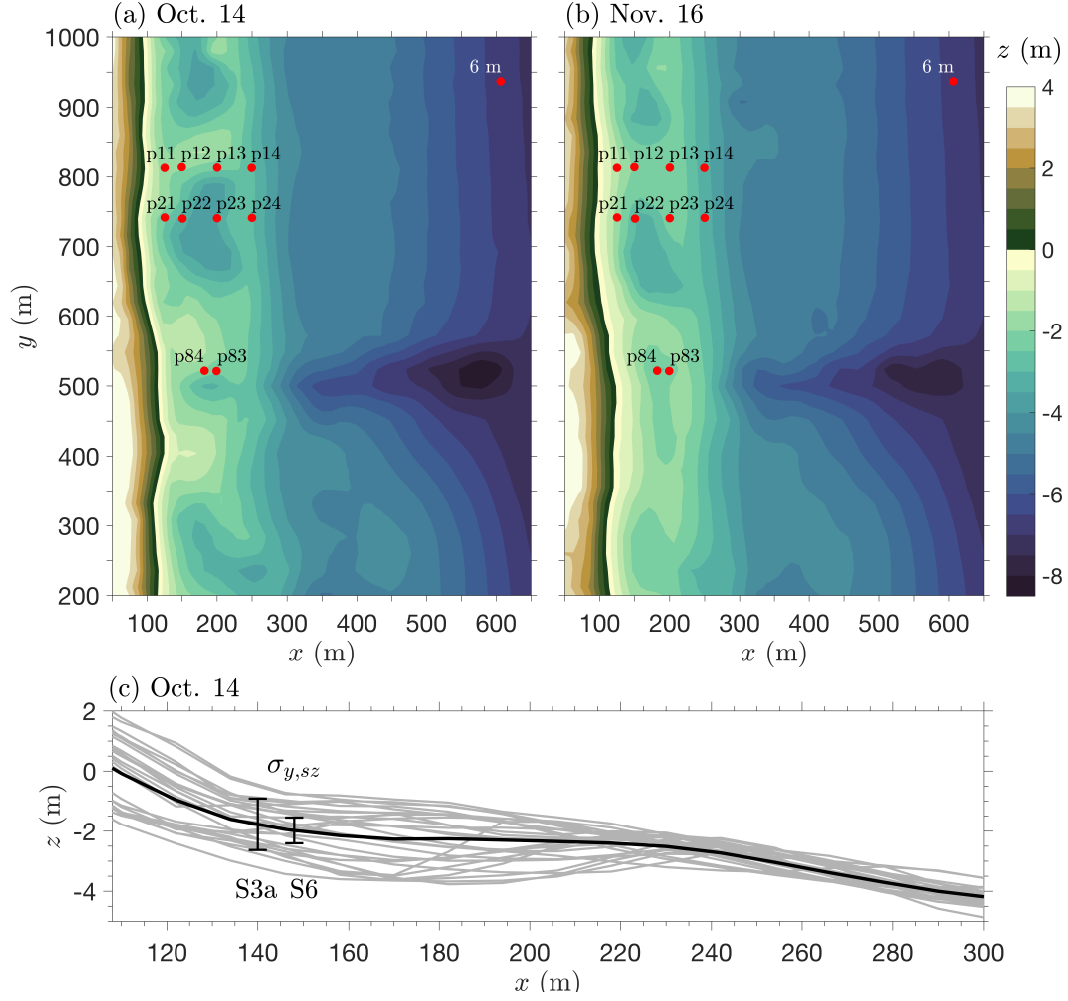


Figure 1. Locations of colocated ADVs and pressure gauges (red symbols) and bathymetry (z , color contours, scale on the right) measured on (a) Oct. 14, 2015 and (b) Nov. 16, 2015 versus cross- (x) and along-shore (y) coordinates. Bathymetry from Oct. and Nov. have alongshore-varying sandbar-trough and terrace systems interrupted by channels. The deep channel at around $y = 500$ m is formed from scour near the FRF pier. (c) Vertical elevation (z) versus cross-shore coordinate (x) for profiles every 45 m in the alongshore (S3a, gray curves) and the alongshore-averaged profile (S7, black curve) for Oct 14. The alongshore standard deviation of the bathymetry ($\sigma_{y,sz}$) in the surf zone is denoted with vertical bars for simulations S3a and S6 (Tables 1, 2).

$y = 600\text{--}750$ m, Figure 1b: $y = 550\text{--}700$ m), variable terraces (e.g., Figure 1a: $y = 750\text{--}825$ m, Figure 1b: $y = 700\text{--}800$ m), and a scoured channel under the FRF pier (Figure 1a,b: $y = 500$ m). Between Oct. 14 and Nov. 16, there was on average about a 10 m shoreward migration of the bar crest at $y = 600\text{--}1100$ m and a southward migration of some bathymetric features, such as the depression from $y = 600 - 750$ m on Oct. 14, which may have migrated to $y = 550 - 700$ by Nov. 16 (Figure 1a,b).

ADV measurements were quality controlled [Elgar *et al.*, 2005] and used to compute hourly bulk current and wave parameters, reported as the average of six 512-second data collections each hour. A frequency-dependent correction for depth using linear wave theory was applied to nearshore pressure measurements to estimate sea-surface elevation statistics [Guza and Thornton, 1980]. Significant wave heights (H_s , 4 times the standard deviation of sea-surface elevation fluctuations for $0.05 < f < 0.30$ Hz) have an estimated error $< 5\%$. The energy-weighted wave angles (θ) and directional spread (σ_θ) were computed for the same frequency range using directional moments [Kuik *et al.*, 1988], and have an estimated error of 5° owing to compass inaccuracies. Incident waves from counter-clockwise (from the north-east) and clockwise (from the south-east) of shore-normal are reported as $\theta > 0^\circ$ and $\theta < 0^\circ$, respectively. The range of the mean water level ($\langle \eta \rangle$, including tides, surge, and other large-scale water-level fluctuations) measured by a NOAA tide gauge ($h = 6$ m, $x, y = 582, 509$ m) varied from -0.6 to 1.0 m. In 11-m water depth, H_s ranged from 0.3 to 2.0 m, θ varied from -45° to 50° , σ_θ was between 25° to 40° , and the peak wave periods (T_p) ranged from 4 to 12 s. In 2-m water depth, wave heights were depth limited, and thus varied tidally, wave directions usually were close to shore-normal, and directional spreads decreased relative to offshore waves. The maximum hourly-average current speeds at a nearshore sensor at $h \approx 2$ m ($x, y = 150, 740$ m), was approximately 0.5 m/s (0.6 m/s) in the cross-shore (along-shore) when $H_s > 1.5$ m.

2.2 Numerical Modeling Testing Framework

Nearshore circulation and wave propagation were simulated using Simulating WAves till SHore (SWASH), a three-dimensional open source non-hydrostatic wave-flow model [Zijlema *et al.*, 2011]. SWASH solves the nonlinear shallow water equations including non-hydrostatic pressure, and conserves temperature, salinity, and suspended sediment [Zijlema and Stelling, 2005]. The second-order finite difference approximations (in time and space) in SWASH improve the computational efficiency, while correcting for frequency dispersion

through the addition of more vertical layers. The steepening wave front is resolved in simulations with sufficient vertical resolution and regarded as a jump-discontinuity in the flow variables (free surface, velocities). Conservation of momentum is enforced across the discontinuity, which enables an energy dissipation rate similar to a hydraulic jump [Smit *et al.*, 2013]. The hydrostatic front approximation that initiates wave breaking based on thresholds also is used in case the vertical gradients are not resolved adequately. Vertical mixing is approximated using a $k - \epsilon$ model, where k is the turbulent kinetic energy per unit mass and ϵ is the dissipation rate of turbulent kinetic energy per unit mass [Launder and Spalding, 1983]. The sensitivity to other approaches for vertical mixing is not explored here [Rijnsdorp *et al.*, 2017, see Appendix A for further details about the model].

SWASH was run on a 2-m-resolution horizontal grid spanning 1500 m alongshore and 900 m cross-shore from the shoreline to $h = 9$ m water depth with 5 vertical layers. Simulations were run with the observed bathymetry interpolated to the model grid with the still water level set to the hour-averaged observed ($h = 6$ m) water elevation ($\langle \eta \rangle$). To allow for north and south periodic boundary conditions, the domain was extended an additional 124 m alongshore on the northern and southern boundaries, converging exponentially to an alongshore-averaged bathymetry. All simulations were conducted for 2 hours with an initial time step of 0.04 seconds and a cycle length (repeated length of the time series realization) of 1 hr. After 1 hr of model spin up, 1-Hz output for the second hour is used for analysis. Further information about the numerical approach and model settings are provided in Appendix A.

The model was forced uniformly along the offshore boundary by a model-generated JONSWAP spectrum based on the observed offshore bulk wave parameters (H_s , T_p , θ , and σ_θ in $h = 11$ m) and a peakedness parameter (γ_J) calibrated to match the observed spectra ($\gamma_J = 1.4 - 1.9$). Errors introduced by applying forcing from an 11-m depth measurement at the 9-m depth model domain boundary are estimated to be small, with refraction resulting in differences of less than 1° in direction and less than 0.01 m in wave height. Bulk wave and current statistics from model simulations with bathymetry derived from the Oct. 14 survey (Figure 1a) are compared with observations for three directionally spread wave conditions (Table 1). Two of the simulations (S1 and S2, observed conditions on Oct 20 10:00 and 15:00 Eastern Daylight Time (EDT)) were selected to compare oblique with shore-normal waves during lower-energy conditions. The third simulation (S3a, observed conditions on Oct 28 00:00 EDT) has higher-energy, normally incident waves. Additionally, the sensitiv-

ity of the simulated nearshore circulation to bathymetry is investigated by repeating the third simulation (S3a) with bathymetry observed on Nov. 16 (S3b, Figure 1b). The surfzone width (L_{sz}) for each simulation is the distance from the alongshore-averaged shoreline position (x_{sl} , set by the mean water elevation) to the outer edge of the surf zone (x_{sz} , beginning of breaker zone), defined as the cross-shore location with the maximum cross-shore gradient in the alongshore-averaged significant wave height, $d\langle H_s \rangle_y / dx$ (Table 1).

The numerical framework and stability of SWASH impacted the selection of the test cases. For conditions with highly oblique, directionally spread waves ($\theta > 20^\circ$, $\sigma_\theta > 30^\circ$), unrealistic alongshore banding of H_s resulted from interference of the limited directional components that could be included in the domain geometry. Additionally, SWASH became unstable in the swash zone for moderate-energy oblique wave conditions ($\theta > 20^\circ$, $H_s > 1$ m). Simulations were forced with a JONSWAP spectrum generated with the bulk wave parameters, and thus time periods with bi-modal wave spectra, including from Oct. 14 10:00 to Oct. 17 23:00 EDT, were not simulated. The stability was compromised and computational time substantially increased when the number of vertical layers was doubled.

Table 1. Simulated test cases forced with observed conditions, including hour-average mean water elevation ($\langle \eta \rangle$) and offshore ($h = 11$ m) significant wave height (H_s), peak wave period (T_p), incident wave angle ($\theta = 0^\circ$ is shore-normal, $\theta < 0^\circ$ indicates waves from the southeast), directional spread (σ_θ), and the JONSWAP gamma parameter (γ_J). Model bathymetry for each simulation was derived from surveys on Oct. 14 or Nov. 16. The surfzone width (L_{sz}) is the distance between the shoreline (x_{sl} , where alongshore-averaged water depth, $\langle h \rangle_y = 0$) and the beginning of wave breaking (x_{sz}).

Sim.	Time of Obs. (EDT)	Bathymetry	$\langle \eta \rangle$ (m)	H_s (m)	T_p (s)	θ ($^\circ$)	σ_θ ($^\circ$)	γ_J	L_{sz}
S1	Oct. 20 10:00	Oct. 14	-0.03	0.62	7.8	-3.4	30.8	1.9	70
S2	Oct. 20 15:00	Oct. 14	0.13	0.51	8.8	-15.0	29.5	1.8	58
S3a	Oct. 28 00:00	Oct. 14	-0.32	1.95	7.1	-2.1	28.6	1.4	146
S3b	Oct. 28 00:00	Nov. 16	-0.32	1.95	7.1	-2.1	28.6	1.4	134

2.3 Vorticity Wavenumber Spectra Analysis

The alongshore length scales of surfzone eddies are quantified with the hour average of 1-Hz alongshore wavenumber spectra of vertical vorticity (with the spatial mean removed) over the second hour of a simulation (3600 - 7200 s). The alongshore wavenumber spectra were computed from depth-averaged vertical vorticity ($S_{\omega\omega}$) and from vertical vorticity at individual elevations ($S_{\omega\omega}(z)$), for alongshore eddy length scales $L \geq 4$ m ($k/2\pi \leq 0.25$ m⁻¹, where k is the wavenumber) at each cross-shore grid location (2-m resolution). Vertical vorticity was estimated from gridded velocity components using a central-difference approach [Patankar, 1980], where vorticity at individual vertical layers was computed from horizontal velocities at time-evolving terrain-following sigma layers interpolated to a grid of fixed elevations. To estimate phase-averaged vorticity, a 60-s moving average is applied to the vertical vorticity prior to computing the wavenumber spectra of vertical vorticity at 1 Hz. The averaging is applied prior to, rather than following, the discrete vorticity estimate to remove apparent instantaneous wave-induced vorticity that is an artifact of the discretization.

Wavenumber spectra were computed for the energetic shore-normal waves (S3a) over the observed alongshore-variable bathymetry (measured Oct. 14, Figure 1a,c, $\sigma_{y,sz} = 0.86$ m) and for four additional simulations (Table 2) with the same forcing as in S3a (Table 1), but with altered alongshore bathymetric variability and wave directional spread. The sensitivity of eddy length scales to the incident wave field (*e.g.*, short-crested wave breaking) is investigated with two simulations with the observed Oct. 14 bathymetry and with half of the observed (S4, $\sigma_{\theta} = 14.3^\circ$) and zero (S5) offshore directional spread. The influence of alongshore bathymetric variability on the distribution of eddy length scales is addressed with two simulations (S6, S7) with the observed offshore directional spread ($\sigma_{\theta} = 28.6^\circ$) and reduced alongshore bathymetric variability. S6 has bathymetry with half of the observed alongshore variability ($\sigma_{y,sz} = 0.43$ m, bathymetric features decreased by half the observed amplitude about the alongshore-average bathymetry, Figure 1c, right vertical bar), and S7 has alongshore-uniform bathymetry set to the alongshore-average of the observed bathymetric profiles ($\sigma_{y,sz} = 0$ m, Figure 1c, thick black curve).

2.4 Very Low-Frequency Velocity Analysis

The very low-frequency (VLF) surfzone currents, defined here as currents in the band $0.003 < f < 0.007$ Hz, were computed with 1-Hz time series along several cross-shore

Table 2. Simulations for the eddy length-scale analysis with the corresponding alongshore bathymetry standard deviation in the surf zone ($\sigma_{y,sz}$), and the offshore directional spread (σ_θ). All other model parameters for each run are consistent with those for S3a (Table 1).

Sim. No.	$\sigma_{y,sz}$ (m)	σ_θ (°)
S3a	0.86	28.6
S4	0.86	14.3
S5	0.86	0
S6	0.43	28.6
S7	0	28.6

transects of the three-dimensional SWASH simulations. Similar to the vorticity estimates at specific elevations, horizontal velocities at sigma layers were interpolated to a fixed vertical grid spanning from near the mean sea-surface to near the bed. Velocities defined as ‘near-surface’ are at the grid point closest to one half of the alongshore-averaged significant wave height below the mean sea-surface elevation. Velocities defined as ‘near-bottom’ are at the grid point closest to 0.03 m above the bed, typically outside of a surface-gravity wave bottom boundary layer. Temporal velocity spectral analyses were performed using a Hanning window period of 512 s with an overlap period of 256 s for a 1-hr cross- (u) and alongshore (v) velocity 1-Hz time series, yielding a $\Delta f = 0.002$ Hz with the lowest bin centered at $f = 0.002$ Hz and 28 DOF. To test the confidence in VLF statistics over the last hour of the 2-hr simulation, simulation S3a and S7 (Table 2) were run for a longer time period (4 hrs with 84 DOF). The statistics from the last hour of the 2-hr simulation (3600 - 7200 s) were similar to statistics from the last 3 hrs of the 4-hr simulation (3600 - 14400 s), justifying that the results are statistically significant for the shorter simulation. When converted to equivalent velocity using the linear finite-depth dispersion relationship, sea-surface elevation spectral levels ($S_{\eta\eta} * g/h$ where g is gravitational acceleration and h is mean water depth) within the VLF band are 1 to 2 orders of magnitude lower than the velocity spectral levels ($S_{uu} + S_{vv}$, e.g., modeled at $x, y = 132, 740$ m in Figure 2, dashed lines indicate the VLF band), indicating that VLF motions are rotational rather than directly forced by sea, swell, or infragravity waves [Lippmann *et al.*, 1999; MacMahan *et al.*, 2010; Feddersen *et al.*, 2011;

Elgar et al., 2019]. The observed and modeled velocity spectral levels at $x, y = 132, 740$ m are similar for infragravity and VLF motions (within the 95% confidence interval).

The VLF spectral densities (S_{uu}, S_{vv}) are computed as the sum of the frequency bins centered at $f = 0.004$ and 0.006 Hz. The squared coherence of the VLF velocity (λ_u^2, λ_v^2) and the phase relative to the near-surface VLF velocity (ϕ_u, ϕ_v , positive and negative phase indicate leading and lagging surface velocities) are computed as the energy weighted average over the $f = 0.004$ and 0.006 Hz bins [Hannan, 1970; Priestely, 1981]. To represent the relative variability of VLF velocities over the water column, $(u_{rms} - u_{0,rms})/u_{0,rms}$ and $(v_{rms} - v_{0,rms})/v_{0,rms}$, the normalized difference between the root mean square (rms) over time of filtered VLF velocities (u_{rms}, v_{rms}) and the near-surface velocity ($u_{0,rms}, v_{0,rms}$), was computed from the band-passed $0.003 < f < 0.007$ Hz velocities [PL64 filter, Rosenfeld, 1983], where greater and less than 0 indicates more and less VLF velocity variance at depth relative to near the surface, respectively.

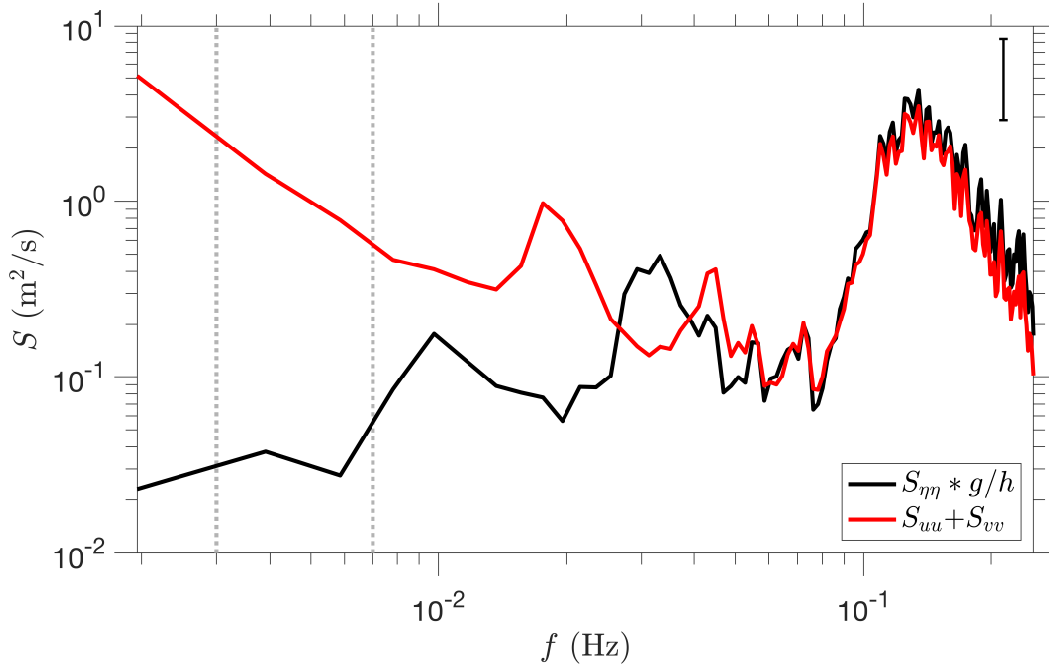


Figure 2. Sea-surface elevation spectral density converted to equivalent velocity ($S_{\eta\eta} * g/h$, black) and the sum of the depth-averaged cross- and alongshore spectral densities (S_{uu}, S_{vv} , red) in the surf zone ($x, y = 132, 740$ m) versus frequency (f). Vortical motion is the dominant energy in the VLF band (between the vertical dashed lines). The vertical bar indicates the 95% confidence interval for 28 DOF.

3 Results

3.1 Observed and Modeled Nearshore Conditions

The capability of SWASH to simulate surfzone circulation on a natural beach is tested by comparing the modeled with the observed hourly bulk wave and current statistics. At the model offshore boundary ($h = 11$ m) for simulations with Oct. 14 bathymetry (S1, S2, S3a, Table 1) the alongshore-averaged $S_{\eta\eta}$ is similar to the observed sea-surface elevation spectra ($S_{\eta\eta}$, Figure 3, black curves). The observed and modeled $S_{\eta\eta}$ also are similar at $h = 6$ m (Figure 3, red curves), with slightly lower energy in the modeled spectra at the peak frequency for lower-energy waves (S1, S2). The differences between the observed and modeled spectra at $h = 6$ m may be associated with differences in the observed and modeled offshore spectrum and boundary conditions (Figure 3, black curves), including the assumption of uniform wave forcing along the offshore boundary, and inaccuracy in modeled physics (*e.g.*, wave transformation, wave-wave interactions, and other nonlinear processes).

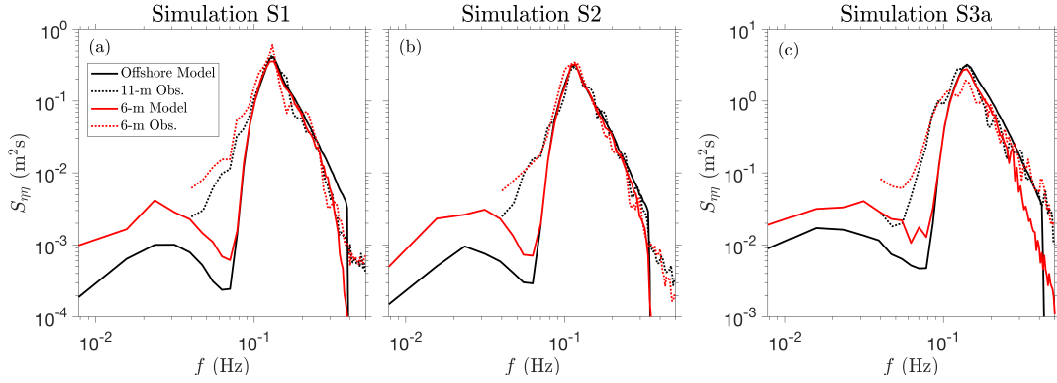


Figure 3. Sea-surface elevation spectral densities ($S_{\eta\eta}$) versus frequency (f) for alongshore-averaged model spectra at the offshore boundary (solid-black curves), observed spectra in 11-m depth (dashed-black curves), and simulated (solid-red curves) and observed (dashed-red curves) spectra in 6-m depth for simulations (a) S1, (b) S2, and (c) S3a. There are 48 DOF in the spectra.

The modeled and observed H_s for simulations with Oct. 14 bathymetry (S1, S2, S3a) have similar patterns, including a reduction in H_s from depth-limited breaking in the surf zone (Figure 4b,d, 5b, x_{SZ} : dashed-white lines) and smaller H_s near the pier due to wave refraction (around $y = 500$ m). Although the model simulates the observed cross-shore pattern of H_s , the modeled H_s is larger than observed (RMSE = 0.28 m, bias = 0.23 m, Figure 4b,d, 5b, colors in circles are darker than in the surrounding area). The positive bias of

the modeled H_s is smaller if the stations near the pier (p84 and p85), where large changes in bathymetry may occur, are not included in the comparison (RMSE=0.21 m, bias = 0.18 m). The similar patterns and positive bias of modeled H_s relative to observations is shown along the cross-shore transect at $y = 741$ m (along stations p21-24, Figure 6a), where the modeled statistics are alongshore-averaged over 90 m ($696 \leq y \leq 786$ m, Figure 6, solid curves). A simulation with higher spatial resolution (1-m) performed for the same conditions as S1 resulted in similar errors between the modeled and observed wave height and velocities. Errors in H_s are larger than results from 3D simulations with small alongshore bathymetric variability [Rijnsdorp *et al.*, 2015], whereas the absolute biases are similar to 2-layer simulations at Duck, NC [Gomes *et al.*, 2016]. The wave breaking parameters, α and β (Appendix A) were set to standard values from the literature and were not tuned to this dataset. Although dissipation due to wave breaking may be improved with higher resolution simulations, increasing the number of vertical layers led to instabilities. Due to the bathymetric uncertainty and a focus on understanding circulation dynamics rather than accurate hindcasting, tuning of the vertical resolution to minimize errors between the observed and modeled H_s was not investigated here.

The observed and simulated hour-averaged velocities include strong offshore-directed cross-shore velocities, $\langle u \rangle$, as part of bathymetric rip-current circulation cells, and along-shore velocities, $\langle v \rangle$, that meander around prominent bathymetric features with weaker $\langle v \rangle$ in the center of circulation cells (*e.g.*, $y = 741$ m, Figure 4a,c, 5a). The modeled depth-averaged velocities are on average higher than the observed velocities (bias = 0.04 m/s), but almost always are within the alongshore range (Figure 6, shaded regions, comparisons with depth-varying velocities at the instrument elevations are similar). For small shore-normal wave conditions (S1), the modeled and observed velocities have similar magnitudes with small differences that may be owing to localized bathymetric variability not resolved by the surveys or to migration of bathymetric features after the Oct. 14 survey (Figure 6b,c). For the moderate-energy shore-normal wave condition (S3a), the strongest modeled $\langle u \rangle$ appear to be shifted in the positive alongshore direction relative to the observations (Figure 5a), which may be due to migration of bathymetric features resulting from strong alongshore currents between Oct. 14 and Oct. 28.

To determine the sensitivity of the H_s and hour-averaged velocity spatial patterns to bathymetric variability, an additional simulation was conducted with bathymetry from Nov. 16 and the moderate-energy shore-normal wave conditions observed on Oct. 28 (S3b, same

423 wave conditions as S3a). Oct 28 is approximately halfway between the dates of two bathymetry
 424 surveys (Figure 1a,b). The modeled $S_{\eta\eta}$ at $h = 6$ m is not sensitive to the survey bathymetry,
 425 but surfzone H_s are smaller in S3b than in S3a, and thus are more similar to observations
 426 (S3a: bias = 0.40 m, S3b: bias = 0.23 m, Figure 6d, compare black with red curves). In S3b,
 427 the position of the modeled circulation features, including the strong offshore-directed ve-
 428 locities, is similar to that of the observations, leading to smaller errors in a point-to-point
 429 comparison (S3a: RMSE = 0.30 m/s, S3b: RMSE = 0.13 m/s, Figure 6e,f).

448 3.2 Vorticity Wavenumber Spectra

449 The cross-shore and vertical variability of eddy length scales on alongshore-variable
 450 bathymetry is not known. Here, the alongshore wavenumber spectra of the modeled vertical
 451 vorticity is considered for shore-normal waves ($H_s = 2$ m) with different directional spreads
 452 (S3a, S4, S5) and alongshore bathymetric variability (S3a, S6, S7, Table 2). The cross-shore
 453 coordinate is normalized by the surfzone width, L_{sz} (Table 1), where $L_{sz} = x_{sz} - x_{sl}$, where
 454 x_{sz} is the position of the outer edge of the surf zone, and x_{sl} is the alongshore-mean position
 455 of the still-water shoreline. Swashzone dynamics, including strong runup and backwash ve-
 456 locities, along an alongshore-varying shoreline may dominate the vorticity field near and in
 457 the swash zone ($0L_{sz} < x - x_{sl} < 0.2L_{sz}$) and are not shown here, where the focus is on the
 458 inner ($0.2L_{sz} < x - x_{sl} < 0.5L_{sz}$) and outer surf zones ($0.5L_{sz} < x - x_{sl} < 1.0L_{sz}$), and just
 459 offshore of the surf zone ($1.0L_{sz} < x - x_{sl} < 1.5L_{sz}$).

470 3.2.1 Cross-Shore Variability of the Alongshore Wavenumber Spectra of Vorticity

471 For simulations conducted with observed Oct. 14 bathymetry ($\sigma_{y,sz} = 0.86$ m) and dif-
 472 ferent offshore directional spreads (S3a, S4, S5), the magnitude of $S_{\omega\omega}$ is largest at large
 473 length scales ($L > 100$ m) and is insensitive to directional spread in the inner surf zone
 474 (Figure 7a). In contrast, in the outer surf zone and immediately outside the surf zone, $S_{\omega\omega}$
 475 has more variance at large length scales for simulations with less directional spread (Figure
 476 7b,c). The magnitude of $S_{\omega\omega}$ at small length scales ($O(10)$ m), hypothesized to be associated
 477 with injection of vorticity from finite-crested breaking waves, is highest for the largest wave
 478 directional spread (S3a) at all cross-shore positions (Figure 7, top row). For the simulation
 479 with the largest directional spread (S3a, $\sigma_\theta = 28.6^\circ$), the magnitude of $S_{\omega\omega}$ at $L < 85$ m
 480 in the outer surf zone, where wave breaking is strong, is larger than the magnitude in the in-

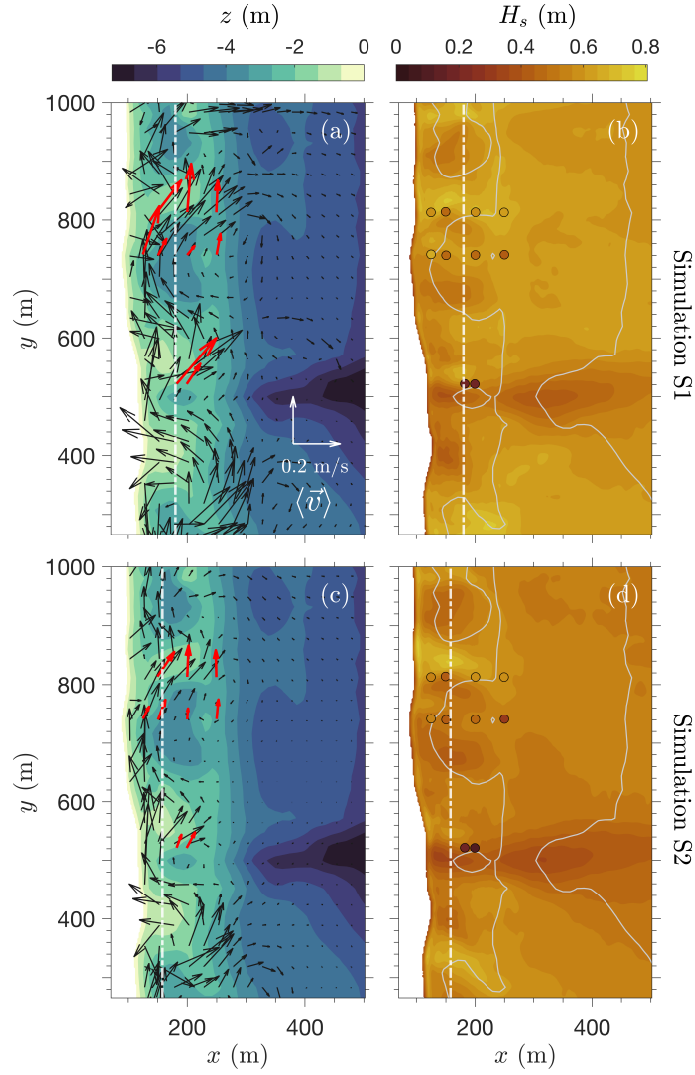


Figure 4. Observed (left: red arrows, right: filled circles) and modeled (left: black arrows, right: color contours) (a,c) hour-averaged depth-averaged velocity, $\langle \vec{v} \rangle$ and (b,d) significant wave height, H_s for small shore-normal (S1, a,b) and oblique (S2, c,d) wave conditions. Bathymetry (left: color contours, right: grey contour curves at 2.5 and 5.0 m depths) and the approximate outer edge of the surf zone (x_{sz} , all panels: dashed-white lines) are shown. Sensor measurements that were removed during quality control are not included here.

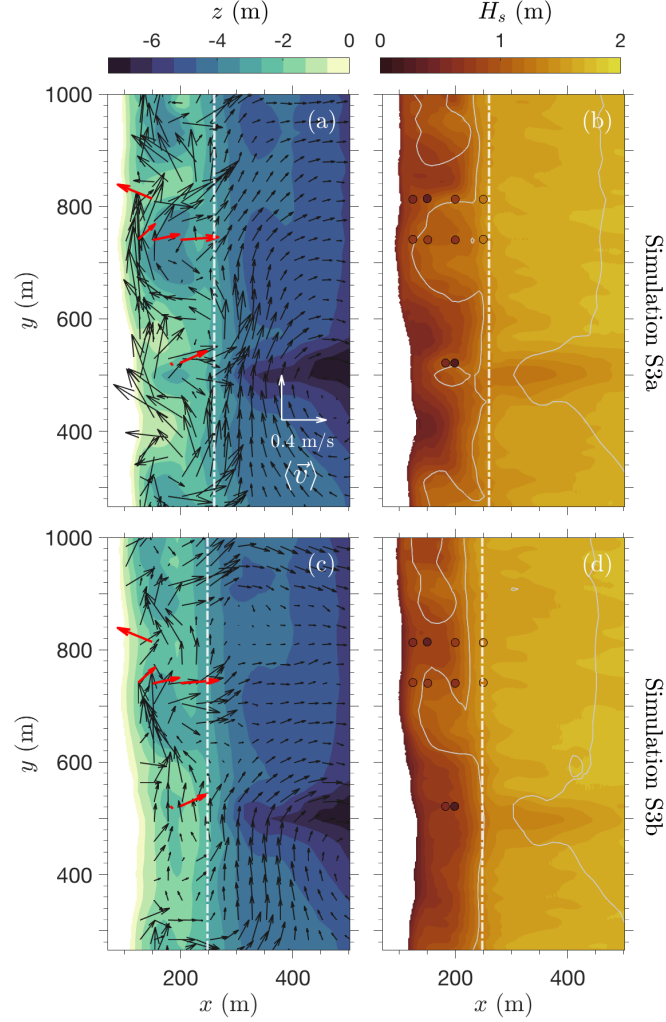


Figure 5. Observed (left: red arrows, right: filled circles) and modeled (left: black arrows, right: color contours) (a,c) hour-averaged depth-averaged velocity, $\langle \vec{v} \rangle$ and (b,d) significant wave height, H_s for moderate-energy shore-normal wave conditions on Oct. 28 with Oct. 14 (S3a, a,b) and Nov. 16 (S3b, c,d) bathymetry. Bathymetry (left: color contours, right: grey contour curves at 2.5 and 5.0 m depth) and the approximate outer edge of the surf zone (x_{sz} , all panels: dashed-white lines) are shown. The $\langle \vec{v} \rangle$ scale (left) and H_s colorbar (right) span approximately twice the range of those in Figure 4.

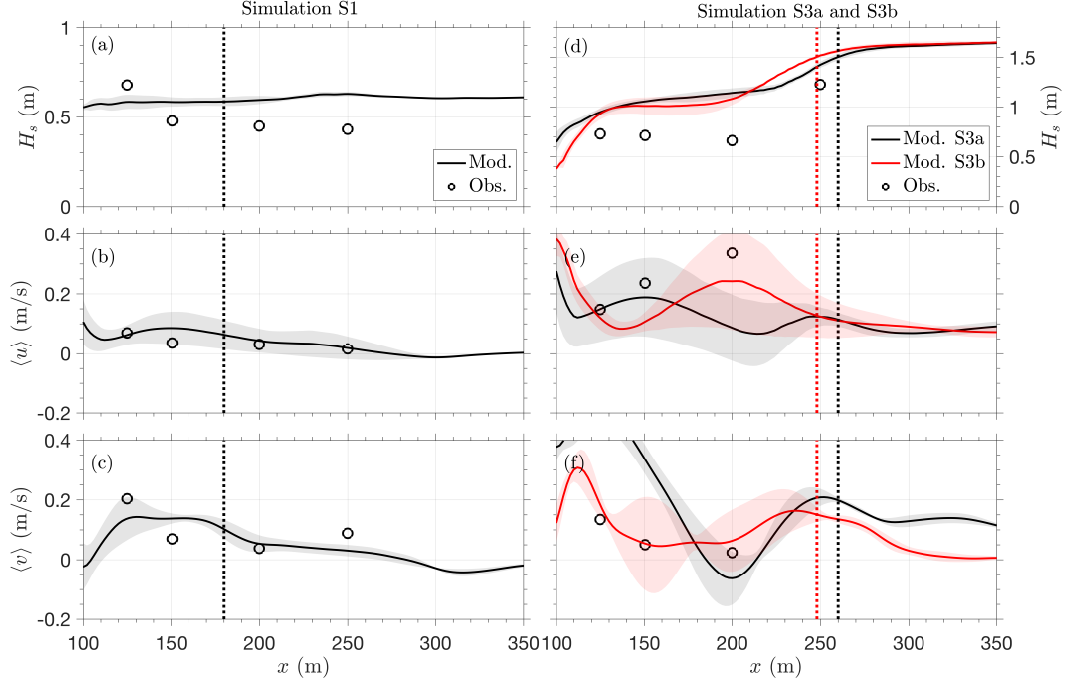


Figure 6. (a,d) Observed (circles) and modeled (curves) significant wave height, H_s and (b,e) 1-hr mean cross-shore, $\langle u \rangle$ and (c,f) alongshore $\langle v \rangle$ velocities along the cross-shore transect at $y = 741$ m (Figure 1) for simulations S1 (left), S3a (right, black), and S3b (right, red). Model results are represented as the cross-shore profiles of 90 m alongshore-averaged (curves) and standard deviation (shaded areas) of wave and current statistics. The black (S1, S3a) and red (S3b) dashed vertical lines are the alongshore-averaged outer edge of the surf zone, x_{sz} .

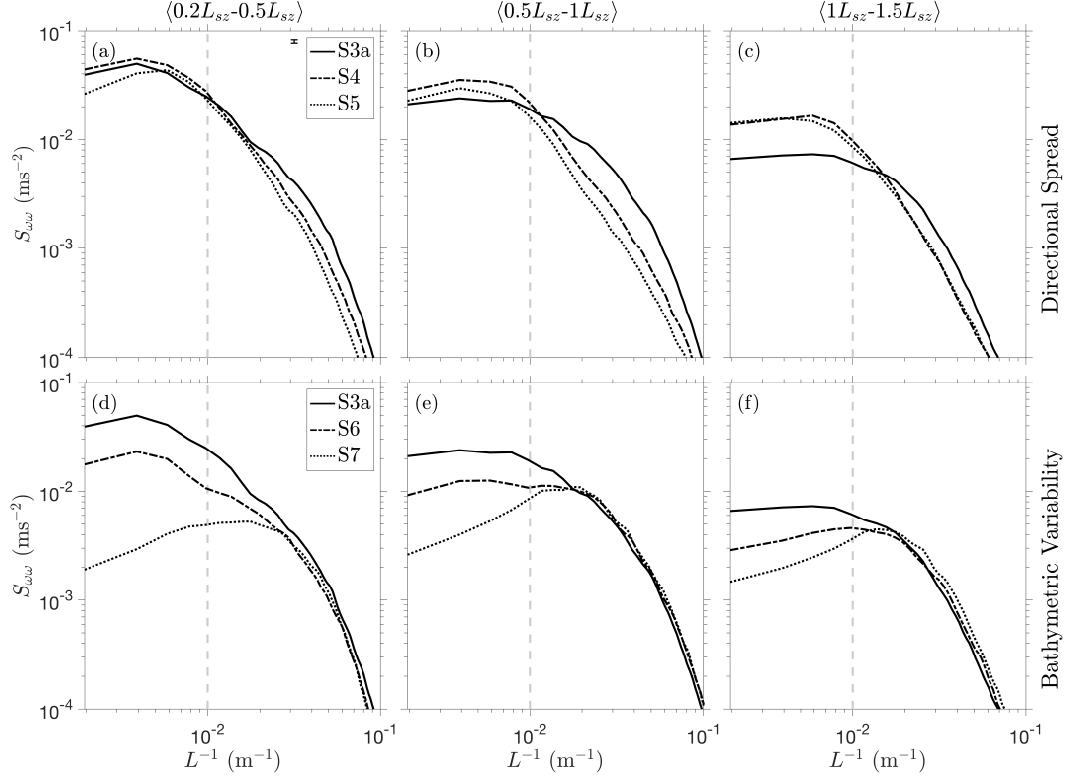


Figure 7. Cross-shore average of the alongshore wavenumber spectra of vorticity ($S_{\omega\omega}$) versus the inverse alongshore length scale (wavenumber divided by 2π , $L^{-1} = k_y/2\pi$, vertical dashed grey lines at $L = 100$ m) for (a,d) the inner surf zone ($0.2L_{sz} < x - x_{sl} < 0.5L_{sz}$), (b,e) the outer surf zone ($0.5L_{sz} < x - x_{sl} < 1.0L_{sz}$), and (c,f) just offshore of the surfzone edge ($1.0L_{sz} < x - x_{sl} < 1.5L_{sz}$) for (a-c) simulations with observed bathymetry and forced with large directional spread (S3a, $\sigma_\theta = 28.6^\circ$, solid curves), half the directional spread (S4, $\sigma_\theta = 14.3^\circ$, dot-dashed curves), and no directional spread (S5, $\sigma_\theta = 0^\circ$, dotted curves), and for (d-f) simulations with directionally spread waves ($\sigma_\theta = 28.6^\circ$) and observed Oct. 15 bathymetry (S3a, $\sigma_{y,sz} = 0.86$ m, solid curves), half the observed alongshore bathymetric variability (S6, $\sigma_{y,sz} = 0.43$ m, dot-dashed curves), and alongshore-averaged bathymetry (S7, $\sigma_{y,sz} = 0$ m, dotted curves). The vertical bar in (a) indicates the 95% confidence interval for 3540 DOF.

ner surf zone and just offshore of the surf zone (Figure 7, top row, compare solid curves at $L^{-1} > 10^{-2} \text{ m}^{-1}$).

For simulations with observed offshore directional spread ($\sigma_\theta = 28.6^\circ$) and differing alongshore bathymetric variability (S3a, S6, S7, Table 2), the variance of vorticity fluctuations at large length scales ($L > 100 \text{ m}$) increases with increasing alongshore bathymetric variability (Figure 7, bottom row). The largest sensitivity to bathymetry of the $S_{\omega\omega}$ magnitude at large length scales occurred in the inner surf zone (Figure 7d), where deep trough and terrace bathymetric features are present. In contrast, the variance of small length-scale eddies ($O(10) \text{ m}$) is similar and relatively independent of alongshore bathymetric variability (Figure 7d-f).

3.2.2 Vertical Variability of the Alongshore Wavenumber Spectra of Vorticity

The cross-shore variability of eddy length scales has been investigated with models that account for the generation of eddies from short-crested wave breaking [Kumar and Feddersen, 2017; O’Dea et al., 2021]. However, the vertical variability of eddy length scales is not known and has not been investigated using a three-dimensional phase-resolving model. Here, the alongshore wavenumber spectra of vertical vorticity at different elevations ($S_{\omega\omega}(z)$), computed with interpolated horizontal velocities, Section 2.3) are used to investigate the vertical variability of eddy length scales in the surf zone for shore-normal waves with Oct. 14 observed (S3a, Figure 8a-c) and alongshore-averaged (S7, Figure 8d-f) bathymetry. The magnitude of $S_{\omega\omega}(z)$ at large length scales ($L > 100 \text{ m}$) is larger at all depths for the alongshore-varying (S3a) than for the alongshore-uniform (S7) bathymetry (compare Figure 8a-c with Figure 8d-f), consistent with the wavenumber spectra computed from the depth-averaged velocities ($S_{\omega\omega}$, Figure 7).

The magnitude of $S_{\omega\omega}(z)$ is nearly depth uniform outside of (not shown) and at the outer edge (Figure 8c,f) of the surf zone, and decays slightly with decreasing vertical elevations, primarily for small length-scale eddies, in the outer surf zone in both examples (Figure 8b,e) and in the inner surf zone for the alongshore-uniform bathymetry (Figure 8d). The vertical dependence of $S_{\omega\omega}(z)$ in the inner surf zone for the alongshore-variable bathymetry is not evaluated here due to the inability to resolve $S_{\omega\omega}(z)$ at elevations that are below the seafloor at some alongshore locations (e.g., $z < -0.75 \text{ m}$ at $0.5L_{sz}$, Figure 8a). For the alongshore-variable bathymetry simulation (S3a), the vorticity variance (the area under

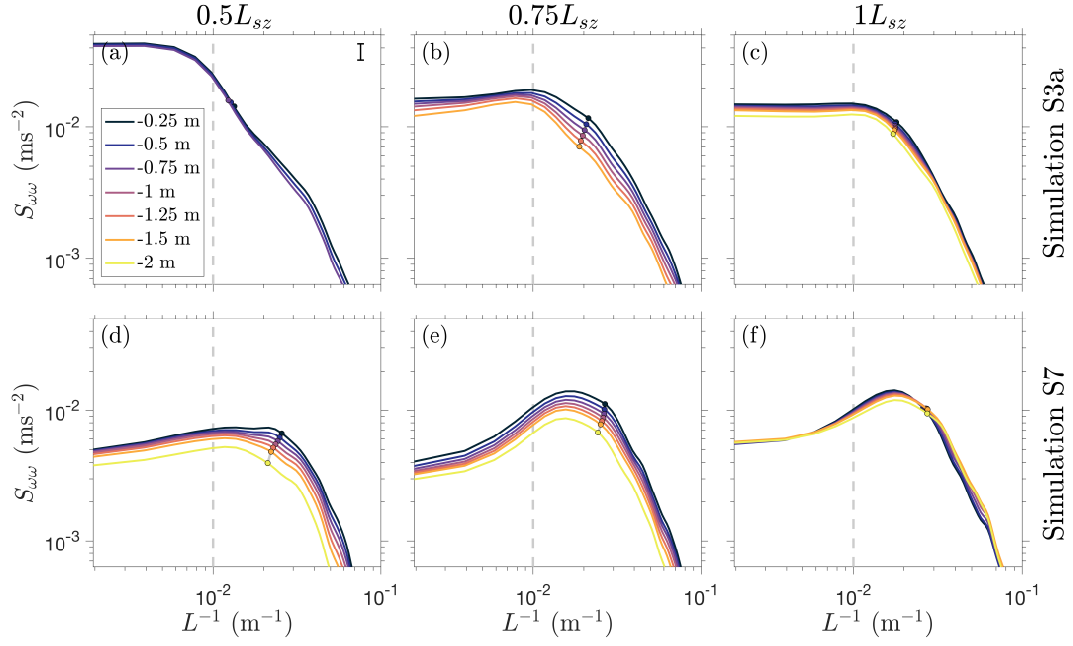


Figure 8. The alongshore wavenumber spectral density of vorticity ($S_{\omega\omega}(z)$) versus the inverse along-shore length scale (wavenumber divided by 2π , $L^{-1} = k_y/2\pi$, vertical dashed grey line at $L = 100$ m) for normalized cross-shore positions (a,d) in the inner surf zone ($x - x_{sl} = 0.5L_{sz}$), (b,e) the outer surf zone ($x - x_{sl} = 0.75L_{sz}$) and (c,f) the outer edge of the surf zone ($x - x_{sl} = 1.0L_{sz}$). At each location, the colored curves (legend inset, lighter curves nearer to the seafloor) are the spectra at 0.25 to 2 m below the mean sea-surface elevation for (a-c) observed bathymetry (S3a) and (d-f) alongshore-uniform bathymetry (S7). The circles (colored by elevation) are at the mean eddy length scale, \bar{L} (centroid). The vertical bar (a) indicates the 95% confidence interval for 354 DOF.

$S_{\omega\omega}(z)$ for small eddy length scales ($L < 100$ m) decays by 36% over 1 m in the water column in the outer surf zone (Figure 8b), whereas the vorticity variance for small length scales decreases by less than 15% over 2 m in the water column at the outer edge of the surf zone (Figure 8c). In the inner and outer surf zone for the alongshore-uniform bathymetry simulation (S7), the vorticity variance from near the surface ($z = -0.25$ m) to the lowest resolved elevation in the water column decays by $\geq 45\%$ for small eddy length scales and $> 25\%$ for large eddy length scales (Figure 8d,e).

Furthermore, the mean eddy length scale, $\bar{L} (= \bar{k}_y/2\pi$, energy-weighted average length scale, the centroid of the spectrum, Figure 8, circles) of $S_{\omega\omega}(z)$ increases with decreasing vertical elevations in the surf zone for nearly all simulations (wavenumber decreases with decreasing vertical elevations, Figure 8b,d,e) and decreases or remains approximately the same over the vertical near the surfzone edge (Figure 8c,f) and just offshore of the surf zone (not shown). For the simulation with the observed bathymetry (S3a), \bar{L} near-surface is ~ 46 m and increases to ~ 53 m over 1.25 m in the water column in the outer surf zone (Figure 8b). Similarly, for the alongshore-uniform bathymetry simulation (S7), \bar{L} is ~ 39 m near the surface and increases to ~ 45 m over 1.5 m in the water column in the inner surf zone (Figure 8d).

3.3 Vertical Structure of Very Low-Frequency Motion

Field observations suggest there may be vertically varying structure of low-frequency eddies in the outer surf zone, but less variation in shallower depths [Lippmann *et al.*, 2016; Henderson *et al.*, 2017]. Here, the very low-frequency (VLF, $0.003 < f < 0.007$, Section 2.3, Figure 2) velocities from the simulation with moderate-energy shore-normal waves and Oct. 14 observed bathymetry (S3a, Figure 1) vary along the barred cross-shore profile ($y = 741$ m) and vertically in the outer surf zone (Figure 9). In the outer surf zone, the change in simulated cross-shore (alongshore) VLF velocities are up to 0.14 m/s (0.12 m/s) over the water column (not shown). The VLF velocity spectral density varies in the cross-shore, with the highest cross-shore VLF spectral density near the bar crest at $x = 220 - 240$ m (Figure 9a) and the highest alongshore VLF spectral density near the shoreline at $x < 100$ m (Figure 9e). The cross- and alongshore spectral densities are similar in magnitude at all locations, except near the bar crest where the cross-shore spectral density is much greater than the alongshore spectral density (Figure 9a,e). The coherence of VLF velocities at different elevations in the water column with those near the surface decreases with distance below the surface, includ-

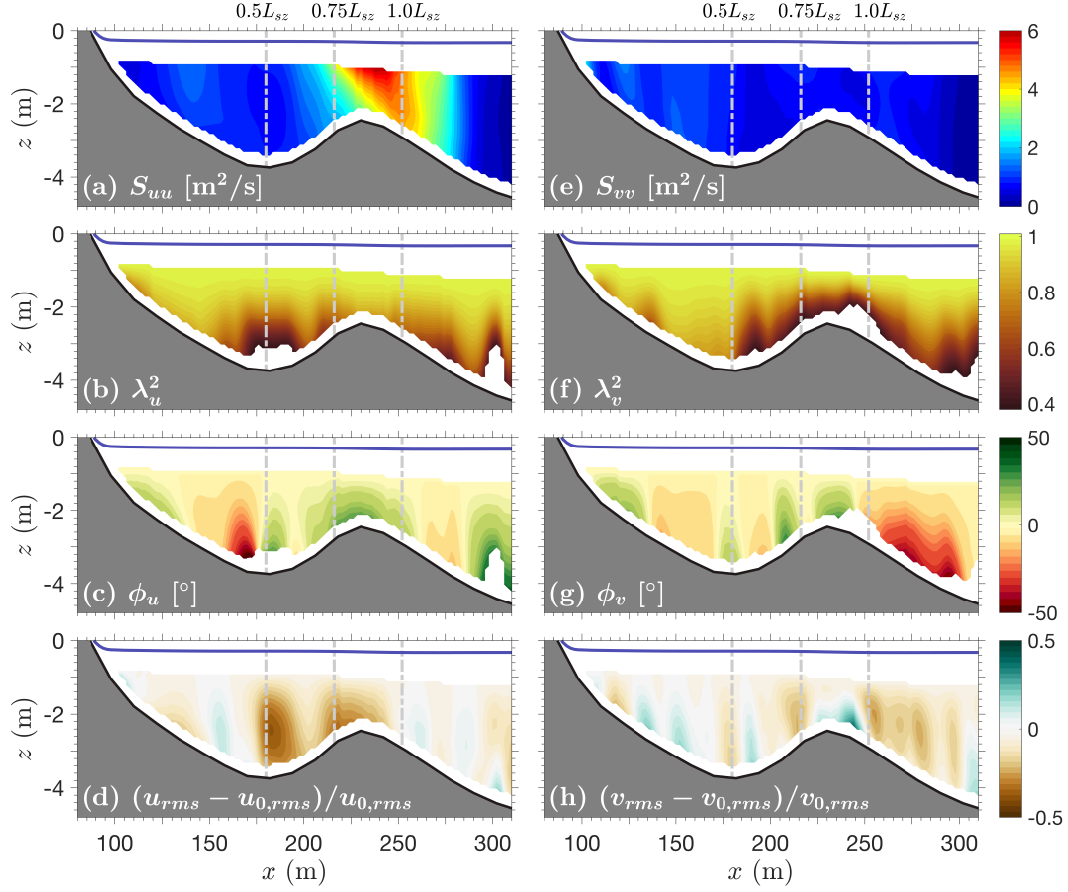


Figure 9. Cross-shore transect for the simulation S3a at $y = 741$ m of the (a-d) cross- and (e-h) along-shore VLF velocity spectral density (a: S_{uu} , e: S_{vv}), squared coherence (b: λ_u^2 , f: λ_v^2), phase shift (c: ϕ_u , g: ϕ_v), and the normalized root-mean-squared (rms) difference (d: $(u_{rms} - u_{0,rms})/u_{0,rms}$, h: $(v_{rms} - v_{0,rms})/v_{0,rms}$) where negative (positive) indicates less (more) variability compared with the surface, with the mean sea-surface elevation (blue) and surfzone regions (dashed grey lines). Values are not shown for coherence squared and phase when the coherence is less than the 95% significance level.

ing near the wave breaking region (around the bar crest, $x = 200 - 270$ m, Figure 9b,f). The VLF phase relative to the phase at the surface changes sign in the cross-shore (Figure 9c,g), indicating that near-bottom velocities alternate between leading and lagging surface velocities. The root-mean-squared (rms) VLF cross-shore velocities decrease with depth in the trough and near the bar crest ($x = 175 - 190$ and $x = 220 - 240$ m, Figure 9d), indicating more variable VLF velocities near the surface onshore of the onset of wave breaking. The rms VLF alongshore velocities have relatively small vertical dependence onshore and offshore of the bar (Figure 9h).

Cross-shore transects at other regions of the S3a domain (*e.g.*, the terraced beach profile at $y \approx 850$ m, Figure 1) have similar vertical dependence in the outer surf zone (*e.g.*, $0.75L_{sz}$), as do VLF velocities with alongshore-uniform bathymetry (S7 simulation, not shown), suggesting that there is vertical variation of VLF velocities in the outer surf zone, with decreasing vertical dependence toward the shore for both the simulated alongshore-uniform and alongshore-varying bathymetry.

4 Discussion

4.1 Cross-Shore Variability of Vorticity Wavenumber Spectra

The length scales of horizontal eddies and their dependence on the incident wave forcing, coupled with the role of surfzone bathymetry, is a focus of recent studies [Feddersen, 2014; Kumar and Feddersen, 2017; O’Dea *et al.*, 2021]. Here, for simulations with varying offshore directional spread (σ_θ) on an alongshore inhomogeneous bathymetry, the vorticity variance, $\sigma_{\omega\omega}^2$ (the area under alongshore wavenumber spectra of depth-averaged vertical vorticity separated for inverse length scales (wavenumbers divided by 2π , $L^{-1} = k_y/2\pi$) on either side of 0.01 m^{-1} , $S_{\omega\omega}$, in Figure 7) at small length scales ($L < 100$ m) increases with directional spread in all cross-shore regions (Figure 10a, circles, squares, triangles, and linear fit with slopes = 3.2, 6.0, and $0.6 \times 10^{-6} \text{ m}^{-1}\text{s}^{-2}$, respectively), consistent with results from previous modeling studies using a depth-integrated wave-resolving Boussinesq model with alongshore-uniform bathymetry [Spydell and Feddersen, 2009; Suanda and Feddersen, 2015] and alongshore-variable bathymetry [O’Dea *et al.*, 2021]. Multiple surfzone processes may contribute to the vorticity variance at small length scales, including generation by directionally spread short-crested breaking waves (*e.g.*, $\sigma_\theta = 28.6^\circ$ in S3a). The small length-scale ($O(10)$ m) vorticity injected during wave breaking may be transferred to

longer length scales through an inverse cascade [Bühler and Jacobson, 2001; Boffetta and Ecke, 2012; Feddersen, 2014; Elgar et al., 2019; Elgar and Raubenheimer, 2020] or dissipated through bottom friction.

In contrast to small length scales, the dependence of large length-scale ($L > 100$ m) vorticity variance on directional spread differs by region within the surf zone, possibly owing to eddy coalescence and pulsations in mean circulation patterns. In the inner surf zone, vorticity variance at large length scales are small and weakly increase with directional spread (Figure 10b, circles and linear fit with slope = $1.3 \times 10^{-6} \text{ m}^{-1} \text{ s}^{-2}$), possibly as a result of the enhancement of the coalescence of small length-scale eddies generated by short-crested wave breaking in the highly variable inner surf zone [Bühler and Jacobson, 2001; Spydell and Feddersen, 2009; Clark et al., 2012] or fluctuations of strong inner surf zone circulation patterns (Figure 5a). In contrast, in the outer surf zone and just offshore of the surf zone, the vorticity variance at large length scales decreases with directional spread (Figure 10b, squares, triangles, and linear fit with slope = $-0.6 \times 10^{-6} \text{ m}^{-1} \text{ s}^{-2}$ and $-2.2 \times 10^{-6} \text{ m}^{-1} \text{ s}^{-2}$, respectively), which may result from fluctuations of strong mean circulation features that extend farther offshore for simulations with variable bathymetry and less directional spread [O’Dea et al., 2021]. Previous funwaveC simulations with alongshore-uniform bathymetry found that the variance at all length scales increased considerably with directional spread in the inner surf zone [Spydell and Feddersen, 2009], whereas for simulations with alongshore-variable bathymetry, the vorticity variance in the inner surf zone increased significantly with directional spread at small length scales and only weakly increased with directional spread at large length scales (Figure 10a,b).

For simulations with a range of alongshore bathymetric variability (the maximum alongshore standard deviation of the seafloor elevation, $\sigma_{y,sz}$), the vorticity variance at small length scales ($L < 100$ m) is independent of bathymetric variability in the outer surf zone and just offshore of the surf zone (Figure 10c, triangles, squares, and linear fits with slopes = -0.2 and $-0.1 \times 10^{-4} \text{ m}^{-1} \text{ s}^{-2}$, respectively), suggesting that small length-scale eddy generation is primarily a function of the incident wave field, rather than the surfzone bathymetric variability. However, in the inner surf zone, higher variance of medium length-scale ($L = 80 - 100$ m) eddies is present in the simulation with observed bathymetry ($\sigma_{y,sz} = 0.86$ m) than in simulations with less alongshore variability (Figure 7d, 10c). The source of this additional variance is unknown, but may be related to instabilities of the mean circulation,

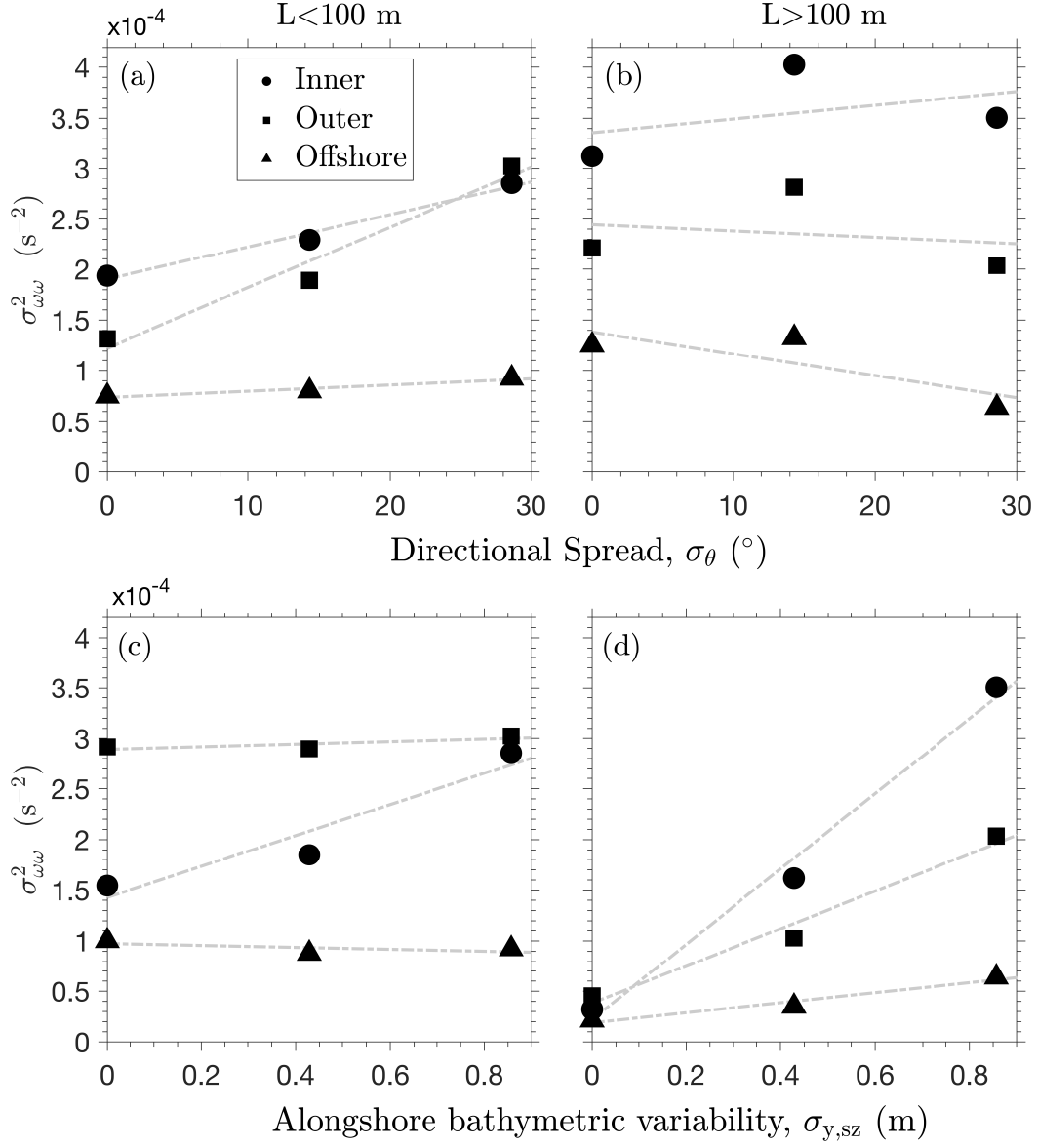


Figure 10. Vorticity variance, $\sigma_{\omega\omega}^2$ versus (a,b) directional spread, σ_θ (S3a, S4, S5) and (c,d) the standard deviation of surfzone bathymetric variability, $\sigma_{y,sz}$ (S3a, S6, S7) for (a,c) small ($L < 100$ m) and (b,d) large ($L > 100$ m) eddy length scales for the inner (circles, $0.2L_{sz} < x - x_{sl} < 0.5L_{sz}$), outer (squares, $0.5L_{sz} < x - x_{sl} < 1.0L_{sz}$), and offshore (triangles, $1.0L_{sz} < x - x_{sl} < 1.5L_{sz}$) of the surf zone. Linear least-squares fits are given by the dashed-grey lines.

which tend to have moderate to long length scales associated with the bathymetric variability [Tabeling *et al.*, 1990; Akkermans *et al.*, 2008; Geiman and Kirby, 2013].

In contrast to the vorticity variance at small length scales, which is not strongly dependent on bathymetry, the eddy variance at large length scales ($L > 100$ m) increases with alongshore bathymetric variability in all regions, particularly in the inner surf zone (Figure 10d, circles and linear fit with slope = $5.0 \times 10^{-4} \text{ m}^{-1} \text{ s}^{-2}$). There is a weaker increase in eddy variance with bathymetric variability in the outer surf zone and offshore of the surf zone (Figure 10d, squares, triangles, and linear fit with slopes = 2.5 and $0.7 \times 10^{-4} \text{ m}^{-1} \text{ s}^{-2}$, respectively). The role of bathymetric variability in controlling surfzone vorticity at large spatial scales, shown here as a function of the cross-shore position in the surf zone and degree of alongshore bathymetric variability, is consistent with previous findings that compared the average variance across the entire surf zone for alongshore-uniform and alongshore-variable bathymetry [O’Dea *et al.*, 2021]. Additionally, the vorticity variance at small and large length scales for alongshore-uniform bathymetry (S7) is greatest in the outer surf zone (Figure 10c,d), in agreement with previous phase-resolved, depth-averaged model results that found a maximum bulk VLF rotational velocity in the outer surf zone for large, directionally spread waves on alongshore uniform bathymetry [Feddersen *et al.*, 2011].

The correlation of large-scale eddies with alongshore bathymetric variability, in contrast to no correlation with directional spread, suggests that bathymetric variability influences large-scale low-frequency fluctuations in the surf zone, possibly owing to enhanced eddy interaction and coalescence in depressions or troughs (Figure 1a) [Bühler and Jacobson, 2001]. In addition, the highly variable observed bathymetry modulates wave breaking patterns, driving meandering mean currents (Figure 5a), which may pulsate at low frequencies and may shed large eddies [MacMahan *et al.*, 2004; Reniers *et al.*, 2007]. Eddy kinetic energy is intensified in the surf zone in simulations with bathymetric variability [Uchiyama *et al.*, 2017; O’Dea *et al.*, 2021]. Elevated eddy kinetic energy also is present outside of the surf zone, where oscillations in bathymetrically driven circulation patterns [*e.g.*, rip current jets, Smith and Largier, 1995; Haller and Dalrymple, 2001] or ejections of surfzone eddies [Feddersen, 2014] may result in higher variance at large eddy length scales.

4.2 Vertical Variability of the Vorticity Wavenumber Spectra

Although previous studies have quantified surfzone eddy variability with alongshore arrays of electromagnetic current meters at one elevation in the water column [Oltman-Shay *et al.*, 1989; Noyes *et al.*, 2004], the depth variability of eddies in the surf zone has been investigated in only a few studies, and no previous numerical modeling experiments have investigated the vertical variability of vortical motion with a fully three-dimensional phase-resolving model. Simulations with phase-averaged models have shown vertical structure of shear instabilities [Newberger and Allen, 2007a,b] and the effect of vortex tilting on the surfzone vorticity budget [Uchiyama *et al.*, 2017]. However, these models do not include wave-forced eddy generation, which is an important source of eddy energy and may influence the vertical structure of eddies [Newberger and Allen, 2007a].

Here, the energy levels of the alongshore wavenumber spectra of the simulated vertical vorticity ($S_{\omega\omega}(z)$) decrease slightly from the surface to the seafloor, particularly for small length-scale eddies, and the mean eddy length scales (centroids of the spectra) increase (Figure 8, circles) in some locations in the nearshore for all simulations, indicating that eddies may exhibit elevation dependence for beaches with uniform or alongshore-varying bathymetry. The change in magnitude and mean length scale of $S_{\omega\omega}(z)$ with location within the water column may be related to length-scale dependent attenuation and the combined effects of bottom boundary layer dynamics, vertical mixing, and the vertical distribution of shear instabilities [Lippmann and Bowen, 2016], which could result in depth variation of eddy stretching and tilting, as seen in three-dimensional phase-averaged ROMS simulations [Uchiyama *et al.*, 2017]. The vertical dependence of $S_{\omega\omega}(z)$ may be sensitive to changes in the vertical eddy viscosity [Lippmann and Bowen, 2016] and the incorporation of wave breaking related turbulence production [Feddersen and Trowbridge, 2005].

Simulations with alongshore-uniform bathymetry exhibit vertical variation at all length scales, whereas simulations with alongshore-variable bathymetry only have vertical variation in the outer surf zone (compare Figure 8a-c with Figure 8d-f), indicating that bathymetric variability may play a role in reducing the vertical dependence of large length-scale eddies. Although there is some vertical variation of eddies at all length-scales on alongshore-uniform beaches (Figure 8d,e), on beaches with alongshore-varying bathymetry the vertical dependence at small length scales decreases somewhat in the outer surf zone (Figure 8b) and is negligible in the inner and outer edge of the surf zone (Figure 8a,c). Thus, whereas

small length-scale eddies may exhibit vertical dependence in the outer surf zone on beaches with large alongshore variability, larger length-scale eddies may be nearly depth-uniform on alongshore-variable bathymetry.

4.3 Vertical Structure of Very Low-Frequency Motion

The three-dimensionality of very low-frequency (VLF) currents, which may impact material exchange and dispersion, is not well documented. Similar to the small number of observations of VLF motion vertical structure [Lippmann *et al.*, 2016; Henderson *et al.*, 2017], VLF motion simulated with SWASH varies in the vertical near the bar crest (Figure 9). Cross-shore energy density decays with depth, with over an 60% drop in squared coherence over the water column, and with large phase shifts near the bottom (up to 50°) relative to near-surface velocities [Lippmann *et al.*, 2016]. Simulated VLF velocities have weak vertical dependence of VLF motions near the outer edge of the surf zone with little vertical variation in shallower depths, broadly consistent with observations [Lippmann *et al.*, 2016; Henderson *et al.*, 2017].

Here, the simulated VLF motion exhibits vertical dependence in the outer surf zone, (*e.g.*, immediately onshore of the bar crest, $0.75L_{sz}$, Figures 8b, 9), with decreasing vertical dependence toward the inner surf zone. Furthermore, simulated VLF velocities are elevation dependent for the terraced profile of S3a at $y \approx 850$ m (not shown), and for alongshore-uniform bathymetry (S7, not shown). A theoretical model for eddy vertical dependence for a scenario with a depth-uniform alongshore mean current, constant eddy viscosity, no incorporation of surface shear stresses from wave breaking, and varying bottom friction [Lippmann and Bowen, 2016] suggests the vertical structure of eddies in the surf zone may result from instabilities and bottom boundary layer dynamics. These solutions, which include bottom friction and linearized lateral momentum advection, suggest that eddy vertical structure may depend on vertical mixing, eddy scales, and the magnitude of shear in a mean alongshore current, but do not address shear in the cross-shore current or the role of variability in wave forcing in a phase-resolved framework.

The analyses here build on previous studies to investigate surfzone eddy dynamics by examining the alongshore length scales at lower frequencies than surface gravity waves [Spydell and Feddersen, 2009; O’Dea *et al.*, 2021] and cross-shore profiles of VLF flows ($0.003 < f < 0.007$ Hz) [Lippmann *et al.*, 2016; Henderson *et al.*, 2017]. The vertical de-

pendence of $S_{\omega\omega}(z)$ and VLF horizontal velocities is largest in the outer surf zone ($0.75L_{sz}$, Figures 8b,e, 9), and decreases toward the shoreline. Near $0.5L_{sz}$, the coherence with near-surface cross-shore flows decreases toward the seafloor (Figure 9b), whereas it was not possible to fully assess the vertical dependence of the alongshore eddy length scales at $0.5L_{sz}$ for the alongshore-variable bathymetry because the varying water depths preclude computing $S_{\omega\omega}(k)$ for $z < 0.75$ m. The vertical dependence of $S_{\omega\omega}(k)$ and VLF velocities may be influenced by vertical eddy viscosity, bottom drag, and absence of breaking-wave-generated turbulence in SWASH simulations. Although simulations suggest that low-frequency motions are primarily two-dimensional with some vertical structure, additional observational and numerical studies are necessary to understand the complex three-dimensional structure of VLF velocities in the surf zone, including the sensitivity of VLF velocities to wave conditions and surfzone bathymetries, and the implications for cross-shore exchange.

5 Conclusions

Simulations with a three-dimensional phase-resolving model (SWASH) reproduce the observed trends in wave transformation and the spatial patterns and magnitudes of the mean alongshore currents and meandering circulation on a barred beach with alongshore-inhomogeneous bathymetry. However, circulation features were sometimes shifted spatially relative to the observations, and the simulated significant wave height was overestimated in the surf zone. The simulated surfzone circulation was sensitive to the bathymetry, which evolved during the field study.

The modeled dynamics include the horizontal and vertically-dependent structure of vortical motion in the surf zone. The alongshore eddy length scales were quantified using the alongshore wavenumber spectra of depth-averaged vorticity for simulations with different wave directional spreads and alongshore bathymetric variability. The variance of small length-scale eddies ($O(10)$ m) increases with directional spread and is independent of alongshore bathymetric variability in the outer surf zone and just offshore of the surf zone, suggesting that vortical motion with short alongshore length scales may be related to the incident wave field, and in particular to forcing by short-crested wave breaking, consistent with previous findings [Spydell and Feddersen, 2009; Suanda and Feddersen, 2015]. The variance of large length-scale eddies ($O(100)$ m) increases with alongshore bathymetric variability, indicating that alongshore bathymetric variability may intensify the formation of large length-scale eddies, in agreement with Bousinessq simulations with variability bathymetry

[O'Dea *et al.*, 2021]. The variance of large length-scale eddies decreases with increasing directional spread in the outer surf zone and just offshore of the surf zone, suggesting that the relationship between directional spread and large length-scale eddies is not well understood, but may be related to instabilities in the stronger mean circulation in cases with less directional spread.

Modeled eddy length scales and low-frequency horizontal velocities were primarily two-dimensional with weak dependence on elevation in the outer surf zone, and occasionally in the inner surf zone for both uniform and alongshore-variable bathymetry. The magnitude of the alongshore wavenumber spectra of vorticity decreased, specifically at small length scales, and the mean length scale (spectral centroid) increased between the surface and the seafloor within the surf zone, whereas the vertical variation at the edge of the surf zone and just outside of the surf zone was small. The horizontal and vertical structures of very low-frequency (VLF) motions have complex patterns, including large drops in coherence and changes in phase between near-surface and subsurface flows. The vertical dependence of VLF velocities decreases from the outer surf zone toward the shoreline, broadly consistent with previous field studies [Lippmann *et al.*, 2016; Henderson *et al.*, 2017]. Further investigation is necessary to understand the complex three-dimensional vertical and horizontal variability of low-frequency motions in the surf zone.

Acknowledgments

We thank the staff of the USACE Field Research Facility, Duck, NC and of the PVLAB at the Woods Hole Oceanographic Institution for helping deploy, maintain, and recover sensors, for providing data from long-term sensors, and for bathymetric surveys. Also, we thank Pieter Smit for assistance with the model setup, and Jim Thomson, Falk Feddersen, and other reviewers for useful comments on the manuscript. Support was provided by the University of Washington Royalty Research Fund, the National Science Foundation, the Office of Naval Research, a National Defense Science and Engineering Graduate Fellowship, a Vannevar Bush Faculty Fellowship, the United States Army Corps of Engineers, the United States Coastal Research Program, Sea Grant, and the WHOI Investment in Science Program.

6 Data Availability Statement

Nearshore ADV data used in this study are available at https://zenodo.org/record/4924900#.YMPevzZKhp_ and bathymetry, water levels, and offshore wave data are pro-

vided by the USACE at <https://frfdataportal.erd.c.dren.mil/>. Model configuration files, MATLAB processing codes, and model output used to produce figures in this paper are available at <https://doi.org/10.5281/zenodo.4141219>.

7 Appendix

A: Model description

Simulating WAVes till SHore (SWASH) is based on an explicit, second-order finite difference method for horizontally staggered grids, and conserves mass and momentum at discrete levels for an incompressible fluid with a constant density, which enables an efficient scheme to simulate individual wave propagation and breaking with high spatio-temporal resolution [Zijlema and Stelling, 2005; Zijlema et al., 2011]. The momentum equations are

$$\frac{\partial u_i}{\partial t} + \frac{\partial u_i u_j}{\partial x_j} = -\frac{1}{\rho} \frac{\partial p_h + p_{nh}}{\partial x_i} + \frac{\partial \tau_{ij}}{\partial x_j} - g \delta_{i3} \quad (\text{A.1})$$

and

$$\frac{\partial u_j}{\partial x_j} = 0 \quad (\text{A.2})$$

where x and u are the position and velocity in a Cartesian coordinate system ($i, j = 1, 2, 3$). Here, t is time, ρ is density, g is gravitational acceleration, τ_{ij} are turbulent stresses, and p_h (p_{nh}) is hydrostatic, $\rho g z$ (non-hydrostatic, $\rho g(\eta - z)$) pressure components. The time evolution of the surface elevation is determined by continuity,

$$\frac{\partial \eta}{\partial t} + \frac{\partial}{\partial x_i} \int_{-h}^{\eta} u_i dz = 0 \quad (\text{A.3})$$

where h is the stationary bottom boundary, η is the moving free-surface, and z is the vertical coordinate ($x_{i=3}$). The surface and bottom kinematic boundary layers constrain particle motion, providing the constraints at the fixed bottom,

$$w|_{z=-h} = -u_i \frac{\partial h}{\partial x_i} \quad (\text{A.4})$$

and the free-surface,

$$w|_{z=\eta} = \frac{\partial \eta}{\partial t} + u_i \frac{\partial \eta}{\partial x_i} \quad (\text{A.5})$$

where w is the vertical velocity ($u_{i=3}$) and there is a constant pressure ($p_h = p_{nh} = 0$) and no surface stresses at the free-surface. The bottom boundary shear stress, τ_b is based on a quadratic friction law, with the drag coefficient, c_f determined from the Manning-Strickler formulation such that

$$c_f = 0.015(k/h)^{1/3} \quad (\text{A.6})$$

where k is the Nikuradse roughness height, set as 1 mm, within the range of values used in previous studies at this cite [Hsu *et al.*, 2006].

The turbulent stresses are obtained from a turbulent viscosity approximation ($\tau_{xx} = \nu_h \frac{\partial u}{\partial x}$, where ν_h is the horizontal eddy viscosity and $\tau_{xz} = \nu_v \frac{\partial u}{\partial z}$, where ν_v is the vertical eddy viscosity) [Smit *et al.*, 2013; Rijnsdorp *et al.*, 2017]. The horizontal eddy viscosity is approximated with the Smagorinsky model with a Smagorinsky constant of 0.1 [Smagorinsky, 1963], and vertical mixing is approximated using the $k - \epsilon$ model, with k the turbulent kinetic energy per unit mass and ϵ the dissipation rate of turbulent kinetic energy per unit mass [Launder and Spalding, 1983]. The vertical eddy viscosity allows for diffusion of this stress into the water column, including coupling between vertical layers, and also increases numerical stability [Smit *et al.*, 2013]. A 10^{-3} m²/s background eddy viscosity was specified to account for unresolved vertical mixing, enhancing stability in the model. This value is small compared with the vertical viscosity computed by the standard $k - \epsilon$ model. Although the breaking-induced turbulence is not directly implemented in SWASH, model simulations have shown that the turbulent kinetic energy below spilling breakers is well predicted [Rijnsdorp *et al.*, 2017].

The simulation stability was improved further by discretization with flux-limited (shock-resolving) vertical advective terms indicated with the first-order upwind scheme. At points where velocity is computed, the water depths are approximated with the Monotonic Upstream-centered Scheme for Conservation Laws limiter (MUSCL), a finite volume method that improves numerical accuracy. Non-hydrostatic pressure gradients in the vertical momentum equations are approximated with the Keller-box scheme [Lam and Simpson, 1976]. Explicit time integration is performed using a specified Courant number between 0.05 and 0.30, and the vertical time integration uses the implicit Euler Scheme.

SWASH simulates wave breaking using a hydrostatic front approximation, similar to disabling dispersive terms in the Boussinesq equations [Tissier *et al.*, 2012; Tonelli and Petti, 2010], by prescribing a hydrostatic pressure distribution in the model around the discontinuity of a breaking wave. The turbulent wave-front is regarded as a sub-grid flow feature where the vertical accelerations are not resolved and the non-hydrostatic pressure is set to zero. The hydrostatic front approximation is initiated when local surface steepness exceeds a fraction of the shallow water celerity,

$$\frac{\partial \eta}{\partial x} > \alpha \sqrt{gh} \quad (\text{A.7})$$

where α is a parameterized value. The spatial persistence of wave breaking is achieved by labeling a mesh-point for hydrostatic computation if the neighboring grid point has been labelled for hydrostatic computation and the local steepness exceeds a fraction of the shallow water celerity (Equation A.7) where the parameterized value is replaced with a coefficient β . In all simulations, wave breaking is controlled with a threshold parameter for initiation of wave breaking at a mesh-point, $\alpha = 0.6$ [Lynett Patrick J., 2006] and for the neighboring mesh-points, $\beta = 0.3$. This approach, combined with the conservation of momentum, leads to appropriate levels of energy dissipation on the front face of a breaking wave [Peregrine, 1983].

References

- Akkermans, R., A. Cieslik, L. Kamp, R. Tieling, H. Clercx, and G. Van Heijst (2008), The three-dimensional structure of an electromagnetically generated dipolar vortex in a shallow fluid layer, *Physics of Fluids*, 20(11), 116,601.
- Allen, J. S., P. A. Newberger, and R. A. Holman (1996), Nonlinear shear instabilities of alongshore currents on plane beaches, *Journal of Fluid Mechanics*, 310, 181–213, doi:10.1017/S0022112096001772.
- Apotsos, A., B. Raubenheimer, S. Elgar, and R. Guza (2008), Wave-driven setup and along-shore flows observed onshore of a submarine canyon, *Journal of Geophysical Research: Oceans*, 113(C7).
- Boehm, A. B., N. S. Ismail, L. M. Sassoubre, and E. A. Andruszkiewicz (2017), Oceans in Peril: Grand Challenges in Applied Water Quality Research for the 21st Century, *Environmental Engineering Science*, 34(1), 3–15, doi:10.1089/ees.2015.0252.
- Boehm, F. R., L. Sandrini-Neto, T. Moens, and P. da Cunha Lana (2016), Sewage input reduces the consumption of rhizophora mangle propagules by crabs in a subtropical mangrove system, *Marine environmental research*, 122, 23–32.
- Boffetta, G., and R. E. Ecke (2012), Two-Dimensional Turbulence, *Annual Review of Fluid Mechanics*, 44(1), 427–451, doi:10.1146/annurev-fluid-120710-101240.
- Bowen, A. J., and R. A. Holman (1989), Shear instabilities of the mean longshore current: 1. Theory, *Journal of Geophysical Research: Oceans*, 94(C12), 18,023–18,030, doi:10.1029/JC094iC12p18023.
- Bowen, A. J., D. L. Inman, and V. P. Simmons (1968), Wave ‘set-down’ and set-Up, *Journal of Geophysical Research*, 73(8), 2569–2577, doi:10.1029/JB073i008p02569.

- Bühler, O., and T. E. Jacobson (2001), Wave-driven currents and vortex dynamics on barred beaches, *Journal of Fluid Mechanics*, *449*, 313–339, doi:10.1017/S0022112001006322.
- Castelle, B., T. Scott, R. Brander, and R. McCarroll (2016), Rip current types, circulation and hazard, *Earth-Science Reviews*, *163*, 1–21.
- Clark, D. B., F. Feddersen, and R. T. Guza (2010), Cross-shore surfzone tracer dispersion in an alongshore current, *Journal of Geophysical Research: Oceans*, *115*(C10), doi:10.1029/2009JC005683.
- Clark, D. B., F. Feddersen, and R. T. Guza (2011), Modeling surf zone tracer plumes: 2. Transport and dispersion, *Journal of Geophysical Research: Oceans*, *116*(C11), doi:10.1029/2011JC007211.
- Clark, D. B., S. Elgar, and B. Raubenheimer (2012), Vorticity generation by short-crested wave breaking, *Geophysical Research Letters*, *39*(24), doi:10.1029/2012GL054034.
- Dalrymple, R. A., J. H. MacMahan, A. J. Reniers, and V. Nelko (2011), Rip Currents, *Annual Review of Fluid Mechanics*, *43*(1), 551–581, doi:10.1146/annurev-fluid-122109-160733.
- de Bakker, A. T. M., M. F. S. Tissier, and B. G. Ruessink (2016), Beach steepness effects on nonlinear infragravity-wave interactions: A numerical study, *Journal of Geophysical Research: Oceans*, *121*(1), 554–570, doi:10.1002/2015JC011268.
- Derakhti, M., J. T. Kirby, F. Shi, and G. Ma (2016), Nhwave: Consistent boundary conditions and turbulence modeling, *Ocean Modelling*, *106*, 121–130.
- Elgar, S., and B. Raubenheimer (2020), Field evidence of inverse energy cascades in the surf zone, *Journal of Physical Oceanography*.
- Elgar, S., B. Raubenheimer, and R. T. Guza (2005), Quality control of acoustic Doppler velocimeter data in the surfzone, *Measurement Science and Technology*, *16*(10), 1889–1893, doi:10.1088/0957-0233/16/10/002.
- Elgar, S., B. Raubenheimer, D. B. Clark, and M. Moulton (2019), Extremely Low Frequency (0.1 to 1.0 mHz) Surf Zone Currents, *Geophysical Research Letters*, *46*(3), 1531–1536, doi:10.1029/2018GL081106.
- Feddersen, F. (2012), Scaling surf zone turbulence, *Geophysical Research Letters*, *39*(18).
- Feddersen, F. (2014), The Generation of Surfzone Eddies in a Strong Alongshore Current, *Journal of Physical Oceanography*, *44*(2), 600–617, doi:10.1175/JPO-D-13-051.1.
- Feddersen, F., and R. Guza (2003), Observations of nearshore circulation: Alongshore uniformity, *Journal of Geophysical Research: Oceans*, *108*(C1), 6–1.

- 900 Feddersen, F., and J. Trowbridge (2005), The effect of wave breaking on surf-zone turbu-
 901 lence and alongshore currents: A modeling study, *Journal of Physical Oceanography*,
 902 35(11), 2187–2203.
- 903 Feddersen, F., R. T. Guza, S. Elgar, and T. H. C. Herbers (1998), Alongshore momentum
 904 balances in the nearshore, *Journal of Geophysical Research: Oceans*, 103(C8), 15,667–
 905 15,676, doi:10.1029/98JC01270.
- 906 Feddersen, F., D. B. Clark, and R. T. Guza (2011), Modeling surf zone tracer plumes: 1.
 907 Waves, mean currents, and low-frequency eddies, *Journal of Geophysical Research*,
 908 116(C11), doi:10.1029/2011JC007210.
- 909 Garcez-Faria, A. F., E. B. Thornton, T. P. Stanton, C. V. Soares, and T. C. Lippmann (1998),
 910 Vertical profiles of longshore currents and related bed shear stress and bottom roughness,
 911 *Journal of Geophysical Research: Oceans*, 103(C2), 3217–3232, doi:10.1029/97JC02265.
- 912 Garcez-Faria, A. F., E. B. Thornton, T. C. Lippmann, and T. P. Stanton (2000), Undertow
 913 over a barred beach, *Journal of Geophysical Research: Oceans*, 105(C7), 16,999–17,010,
 914 doi:10.1029/2000JC900084.
- 915 Geiman, J. D., and J. T. Kirby (2013), Unforced Oscillation of Rip-Current Vortex Cells,
 916 *Journal of Physical Oceanography*, 43(3), 477–497, doi:10.1175/JPO-D-11-0164.1.
- 917 Gomes, E. R., R. P. Mulligan, K. L. Brodie, and J. E. McNinch (2016), Bathymetric control
 918 on the spatial distribution of wave breaking in the surf zone of a natural beach, *Coastal*
 919 *Engineering*, 116, 180–194, doi:10.1016/j.coastaleng.2016.06.012.
- 920 Guza, R. T., and E. B. Thornton (1980), Local and shoaled comparisons of sea surface el-
 921 evations, pressures, and velocities, *Journal of Geophysical Research: Oceans*, 85(C3),
 922 1524–1530, doi:10.1029/JC085iC03p01524.
- 923 Haller, M. C., and R. A. Dalrymple (2001), Rip current instabilities, *Journal of Fluid Me-*
 924 *chanics*, 433, 161–192, doi:10.1017/S0022112000003414.
- 925 Haller, M. C., U. Putrevu, J. Oltman-Shay, and R. A. Dalrymple (1999), Wave group forcing
 926 of low frequency surf zone motion, *Coastal engineering journal*, 41(02), 121–136.
- 927 Hally-Rosendahl, K., and F. Feddersen (2016), Modeling surfzone to inner-shelf tracer ex-
 928 change, *Journal of Geophysical Research: Oceans*, 121(6), 4007–4025, doi:10.1002/
 929 2015JC011530.
- 930 Hannan, E. (1970), Multiple time series, Wiley, p. 536.
- 931 Hansen, J. E., B. Raubenheimer, J. H. List, and S. Elgar (2015), Modeled alongshore circula-
 932 tion and force balances onshore of a submarine canyon, *Journal of Geophysical Research:*

- 933 *Oceans*, 120(3), 1887–1903.
- 934 Henderson, S. M., J. Arnold, H. T. Özkan-Haller, and S. A. Solovitz (2017), Depth Depen-
 935 dence of Nearshore Currents and Eddies, *Journal of Geophysical Research: Oceans*,
 936 122(11), 9004–9031, doi:10.1002/2016JC012349.
- 937 Hsu, T.-J., S. Elgar, and R. Guza (2006), Wave-induced sediment transport and onshore sand-
 938 bar migration, *Coastal Engineering*, 53(10), 817–824.
- 939 Kraichnan, R. H. (1967), Inertial Ranges in Two-Dimensional Turbulence, *The Physics of*
 940 *Fluids*, 10(7), 1417–1423, doi:10.1063/1.1762301.
- 941 Kuik, A., G. P. Van Vledder, and L. Holthuijsen (1988), A method for the routine analysis of
 942 pitch-and-roll buoy wave data, *Journal of physical oceanography*, 18(7), 1020–1034.
- 943 Kumar, N., and F. Feddersen (2017), The Effect of Stokes Drift and Transient Rip Currents
 944 on the Inner Shelf. Part I: No Stratification, *Journal of Physical Oceanography*, 47(1),
 945 227–241, doi:10.1175/JPO-D-16-0076.1.
- 946 Kumar, N., G. Voulgaris, J. C. Warner, and M. Olabarrieta (2012), Implementation of
 947 the vortex force formalism in the coupled ocean-atmosphere-wave-sediment transport
 948 (COAWST) modeling system for inner shelf and surf zone applications, *Ocean Modelling*,
 949 47, 65–95, doi:10.1016/j.ocemod.2012.01.003.
- 950 Lam, D. C. L., and R. B. Simpson (1976), Centered differencing and the box scheme for
 951 diffusion convection problems, *Journal of Computational Physics*, 22(4), 486–500, doi:
 952 10.1016/0021-9991(76)90045-0.
- 953 Lauder, B. E., and D. B. Spalding (1983), The numerical computation of turbulent flows,
 954 in *Numerical prediction of flow, heat transfer, turbulence and combustion*, pp. 96–116,
 955 Elsevier.
- 956 Lentz, S. J., and M. R. Fewings (2012), The wind-and wave-driven inner-shelf circulation,
 957 *Annual review of marine science*, 4, 317–343.
- 958 Lippmann, T. C., and A. J. Bowen (2016), The Vertical Structure of Low-Frequency Motions
 959 in the Nearshore. Part II: Theory, *Journal of Physical Oceanography*, 46(12), 3713–3727,
 960 doi:10.1175/JPO-D-16-0015.1.
- 961 Lippmann, T. C., T. H. C. Herbers, and E. B. Thornton (1999), Gravity and Shear Wave Con-
 962 tributions to Nearshore Infragravity Motions, *Journal of Physical Oceanography*, 29(2),
 963 231–239, doi:10.1175/1520-0485(1999)029<0231:GASWCT>2.0.CO;2.
- 964 Lippmann, T. C., E. B. Thornton, and T. P. Stanton (2016), The Vertical Structure of Low-
 965 Frequency Motions in the Nearshore. Part I: Observations, *Journal of Physical Oceanog-*

- 966 *raphy*, 46(12), 3695–3711, doi:10.1175/JPO-D-16-0014.1.
- 967 Long, J. W., and H. T. Özkan Haller (2009), Low-frequency characteristics of wave
 968 group–forced vortices, *Journal of Geophysical Research*, 114(C8), doi:10.1029/
 969 2008JC004894.
- 970 Longuet-Higgins, M. S. (1970), Longshore currents generated by obliquely incident sea
 971 waves: 1, *Journal of Geophysical Research (1896-1977)*, 75(33), 6778–6789, doi:
 972 10.1029/JC075i033p06778.
- 973 Longuet-Higgins, M. S., and R. w. Stewart (1964), Radiation stresses in water waves; a phys-
 974 ical discussion, with applications, *Deep Sea Research and Oceanographic Abstracts*,
 975 11(4), 529–562, doi:10.1016/0011-7471(64)90001-4.
- 976 Lynett Patrick J. (2006), Nearshore Wave Modeling with High-Order Boussinesq-Type Equa-
 977 tions, *Journal of Waterway, Port, Coastal, and Ocean Engineering*, 132(5), 348–357, doi:
 978 10.1061/(ASCE)0733-950X(2006)132:5(348).
- 979 MacMahan, J. H., A. J. H. M. Reniers, E. B. Thornton, and T. P. Stanton (2004), Infragravity
 980 rip current pulsations, *Journal of Geophysical Research: Oceans*, 109(C1), doi:10.1029/
 981 2003JC002068.
- 982 MacMahan, J. H., E. B. Thornton, and A. J. H. M. Reniers (2006), Rip current review,
 983 *Coastal Engineering*, 53(2), 191–208, doi:10.1016/j.coastaleng.2005.10.009.
- 984 MacMahan, J. H., A. J. H. M. Reniers, and E. B. Thornton (2010), Vortical surf zone ve-
 985 locity fluctuations with 0(10) min period, *Journal of Geophysical Research*, 115(C6),
 986 C06,007, doi:10.1029/2009JC005383.
- 987 Morgan, S. G., A. L. Shanks, J. H. MacMahan, A. J. Reniers, and F. Feddersen (2018),
 988 Planktonic subsidies to surf-zone and intertidal communities, *Annual review of marine*
 989 *science*, 10, 345–369.
- 990 Moulton, M., S. Elgar, B. Raubenheimer, J. C. Warner, and N. Kumar (2017), Rip currents
 991 and alongshore flows in single channels dredged in the surf zone, *Journal of Geophysical*
 992 *Research: Oceans*, 122(5), 3799–3816, doi:10.1002/2016JC012222.
- 993 Newberger, P. A., and J. S. Allen (2007a), Forcing a three-dimensional, hydrostatic,
 994 primitive-equation model for application in the surf zone: 2. Application to DUCK94,
 995 *Journal of Geophysical Research: Oceans*, 112(C8), doi:10.1029/2006JC003474.
- 996 Newberger, P. A., and J. S. Allen (2007b), Forcing a three-dimensional, hydrostatic,
 997 primitive-equation model for application in the surf zone: 1. Formulation, *Journal of Geo-*
 998 *physical Research: Oceans*, 112(C8), doi:10.1029/2006JC003472.

- 999 Noyes, T. J., R. Guza, S. Elgar, and T. Herbers (2004), Field observations of shear waves in
1000 the surf zone, *Journal of Geophysical Research*, 109(C1), doi:10.1029/2002JC001761.
- 1001 O’Dea, A., N. Kumar, and M. C. Haller (2021), Simulations of the surf zone eddy field and
1002 cross-shore exchange on a non-idealized bathymetry, *Journal of Geophysical Research:*
1003 *Oceans*, doi:10.1029/2020JC016619.
- 1004 Oltman-Shay, J., P. A. Howd, and W. A. Birkemeier (1989), Shear instabilities of the mean
1005 longshore current: 2. Field observations, *Journal of Geophysical Research: Oceans*,
1006 94(C12), 18,031–18,042, doi:10.1029/JC094iC12p18031.
- 1007 Patankar, S. V. (1980), Numerical heat transfer and fluid flow, hemisphere publ, *Corp., New*
1008 *York*, 58.
- 1009 Peregrine, D. (1998), Surf Zone Currents, *Theoretical and Computational Fluid Dynamics*,
1010 10(1), 295–309, doi:10.1007/s001620050065.
- 1011 Peregrine, D. H. (1983), Water waves, nonlinear Schrödinger equations and their solutions,
1012 *The ANZIAM Journal*, 25(1), 16–43, doi:10.1017/S0334270000003891.
- 1013 Plant, N. G., K. T. Holland, and J. A. Puleo (2002), Analysis of the scale of errors in
1014 nearshore bathymetric data, *Marine Geology*, 191(1), 71–86, doi:10.1016/S0025-3227(02)
1015 00497-8.
- 1016 Priestely, M. (1981), Spectral analysis and time series, *Academic Press*, p. 890.
- 1017 Putrevu, U., J. Oltman-Shay, and I. A. Svendsen (1995), Effect of alongshore nonuniformities
1018 on longshore current predictions, *Journal of Geophysical Research: Oceans*, 100(C8),
1019 16,119–16,130, doi:10.1029/95JC01459.
- 1020 Raubenheimer, B., R. T. Guza, and S. Elgar (2001), Field observations of wave-driven set-
1021 down and setup, *Journal of Geophysical Research: Oceans*, 106(C3), 4629–4638, doi:
1022 10.1029/2000JC000572.
- 1023 Reniers, A. J. H. M., E. B. Thornton, T. P. Stanton, and J. A. Roelvink (2004a), Vertical flow
1024 structure during Sandy Duck: observations and modeling, *Coastal Engineering*, 51(3),
1025 237–260, doi:10.1016/j.coastaleng.2004.02.001.
- 1026 Reniers, A. J. H. M., J. A. Roelvink, and E. B. Thornton (2004b), Morphodynamic model-
1027 ing of an embayed beach under wave group forcing, *Journal of Geophysical Research:*
1028 *Oceans*, 109(C1), doi:10.1029/2002JC001586.
- 1029 Reniers, A. J. H. M., J. H. MacMahan, E. B. Thornton, and T. P. Stanton (2007), Modeling
1030 of very low frequency motions during RIPEX, *Journal of Geophysical Research: Oceans*,
1031 112(C7), doi:10.1029/2005JC003122.

- Rijnsdorp, D. P., P. B. Smit, and M. Zijlema (2012), Non-hydrostatic modelling of infragravity waves using swash, *Coastal Engineering Proceedings*, 1(33), 27, doi:10.9753/icce.v33.currents.27.
- Rijnsdorp, D. P., P. B. Smit, and M. Zijlema (2014), Non-hydrostatic modelling of infragravity waves under laboratory conditions, *Coastal Engineering*, 85, 30–42, doi:10.1016/j.coastaleng.2013.11.011.
- Rijnsdorp, D. P., G. Ruessink, and M. Zijlema (2015), Infragravity-wave dynamics in a barred coastal region, a numerical study, *Journal of Geophysical Research: Oceans*, 120(6), 4068–4089, doi:10.1002/2014JC010450.
- Rijnsdorp, D. P., P. B. Smit, M. Zijlema, and A. J. H. M. Reniers (2017), Efficient non-hydrostatic modelling of 3d wave-induced currents using a subgrid approach, *Ocean Modelling*, 116, 118–133, doi:10.1016/j.ocemod.2017.06.012.
- Rosenfeld, L. (1983), Code-1: Moored array and large-scale data report, *Woods Hole Oceanographic Institution Tech. Rep.*, pp. 83–23.
- Ruessink, B., J. Miles, F. Feddersen, R. Guza, and S. Elgar (2001), Modeling the alongshore current on barred beaches, *Journal of Geophysical Research: Oceans*, 106(C10), 22,451–22,463.
- Ruju, A., J. L. Lara, and I. J. Losada (2014), Numerical analysis of run-up oscillations under dissipative conditions, *Coastal Engineering*, 86, 45–56, doi:10.1016/j.coastaleng.2014.01.010.
- Shanks, A. L., S. G. Morgan, J. MacMahan, and A. J. H. M. Reniers (2010), Surf zone physical and morphological regime as determinants of temporal and spatial variation in larval recruitment, *Journal of Experimental Marine Biology and Ecology*, 392(1), 140–150, doi:10.1016/j.jembe.2010.04.018.
- Simons, R. R., T. J. Grass, and M. Mansour-Tehrani (1992), Bottom shear stresses in the boundary layers under waves and currents crossing at right angles, *Coastal Engineering Proceedings*, 1(23), doi:10.9753/icce.v23.p.
- Smagorinsky, J. (1963), General circulation experiments with the primitive equations, *Monthly Weather Review*, 91(3), 99–164, doi:10.1175/1520-0493(1963)091<0099:GCEWTP>2.3.CO;2.
- Smit, P., M. Zijlema, and G. Stelling (2013), Depth-induced wave breaking in a non-hydrostatic, near-shore wave model, *Coastal Engineering*, 76, 1–16, doi:10.1016/j.coastaleng.2013.01.008.

- 1065 Smit, P., T. Janssen, L. Holthuijsen, and J. Smith (2014), Non-hydrostatic modeling of surf
1066 zone wave dynamics, *Coastal Engineering*, 83, 36–48, doi:10.1016/j.coastaleng.2013.09.
1067 005.
- 1068 Smith, J. A., and J. L. Largier (1995), Observations of nearshore circulation: Rip currents,
1069 *Journal of Geophysical Research: Oceans*, 100(C6), 10,967–10,975.
- 1070 Smith, J. M., S. Bak, T. Hesser, M. A. Bryant, and C. Massey (2017), Frf wave test bed and
1071 bathymetry inversion, *Coastal Engineering Proceedings*, 1(35), 22, doi:10.9753/icce.v35.
1072 waves.22.
- 1073 Spydell, M., and F. Feddersen (2009), Lagrangian Drifter Dispersion in the Surf Zone: Di-
1074 rectionally Spread, Normally Incident Waves, *Journal of Physical Oceanography*, 39(4),
1075 809–830, doi:10.1175/2008JPO3892.1.
- 1076 Stive, M. J. F., and H. G. Wind (1982), A study of radiation stress and set-up in the nearshore
1077 region, *Coastal Engineering*, 6(1), 1–25, doi:10.1016/0378-3839(82)90012-6.
- 1078 Stoner, N., and M. Dorfman (2007), Testing the waters: a guide to water quality at vacation
1079 beaches, *Natural Resources Defense Council*, 8(2010), 12.
- 1080 Suanda, S. H., and F. Feddersen (2015), A self-similar scaling for cross-shelf exchange
1081 driven by transient rip currents, *Geophysical Research Letters*, 42(13), 5427–5434, doi:
1082 10.1002/2015GL063944.
- 1083 Tabeling, P., O. Cardoso, and B. Perrin (1990), Chaos in a linear array of vortices, *Journal of*
1084 *Fluid Mechanics*, 213, 511–530.
- 1085 Tissier, M., P. Bonneton, F. Marche, F. Chazel, and D. Lannes (2012), A new approach to
1086 handle wave breaking in fully non-linear Boussinesq models, *Coastal Engineering*, 67,
1087 54–66, doi:10.1016/j.coastaleng.2012.04.004.
- 1088 Tonelli, M., and M. Petti (2010), Finite volume scheme for the solution of 2d extended
1089 Boussinesq equations in the surf zone, *Ocean Engineering*, 37(7), 567–582, doi:10.1016/j.
1090 oceaneng.2010.02.004.
- 1091 Uchiyama, Y., J. C. McWilliams, and A. F. Shchepetkin (2010), Wave–current interaction in
1092 an oceanic circulation model with a vortex-force formalism: Application to the surf zone,
1093 *Ocean Modelling*, 34(1), 16–35, doi:10.1016/j.ocemod.2010.04.002.
- 1094 Uchiyama, Y., J. C. McWilliams, and C. Akan (2017), Three-dimensional transient rip cur-
1095 rents: Bathymetric excitation of low-frequency intrinsic variability: 3-D TRANSIENT
1096 RIP CURRENTS, *Journal of Geophysical Research: Oceans*, 122(7), 5826–5849, doi:
1097 10.1002/2017JC013005.

- 1098 Visser, P. J. (1986), Wave basin experiments on bottom friction due to current and waves,
1099 *Coastal Engineering Proceedings*, 1(20), doi:10.9753/icce.v20.%p.
- 1100 Warner, J. C., B. Armstrong, R. He, and J. B. Zambon (2010), Development of a Coupled
1101 Ocean–Atmosphere–Wave–Sediment Transport (COAWST) Modeling System, *Ocean*
1102 *Modelling*, 35(3), 230–244, doi:10.1016/j.ocemod.2010.07.010.
- 1103 Zijlema, M., and G. S. Stelling (2005), Further experiences with computing non-hydrostatic
1104 free-surface flows involving water waves, *International Journal for Numerical Methods in*
1105 *Fluids*, 48(2), 169–197, doi:10.1002/flid.821.
- 1106 Zijlema, M., G. Stelling, and P. Smit (2011), SWASH: An operational public domain code
1107 for simulating wave fields and rapidly varied flows in coastal waters, *Coastal Engineering*,
1108 58(10), 992–1012, doi:10.1016/j.coastaleng.2011.05.015.